Enhancement of Nighttime Fire Detection and Combustion Efficiency Characterization Using Suomi-NPP and NOAA-20 VIIRS Instruments

Meng Zhou, Jun Wang, Lorena Castro Garcia, Xi Chen, Arlindo M. da Silva, Zhuosen Wang, Miguel O. Román, Edward J. Hyer, and Steven D. Miller

Abstract— **We present the second-generation FIre Light Detection Algorithm (FILDA-2), which includes advances in fire detection and retrievals of radiative power (FRP), fire visible energy fraction (VEF), and fire modified combustion efficiency (MCE) at nighttime from the holistic use of multiple-spectral radiances measured by the visible infrared imaging radiometer suite (VIIRS) aboard Suomi-NPP (VNP) and National Oceanic and Atmospheric Administration (NOAA)-20/joint polar satellite system (JPSS)-1 (VJ1) satellites. Key enhancements include: 1) a new fast algorithm that maps VIIRS day/night band (DNB) radiances to the pixel footprints of VIIRS moderate (M) and imagery (I) bands; 2) identification of potential fire pixels through the use of the DNB anomalies and I-band thermal anomalies; 3) dynamic thresholds for contextual testing of fire pixels; and 4) pixel-specific estimates of FRP, VEF, and MCE. The global benchmark test demonstrates that FILDA-2 can detect approximately 25%–30% smaller and cooler fires than the operational VIIRS active fire 375-m I-band algorithm with the added benefit of providing daily global pixel-level characterizations of MCE for nighttime surface fires. The MCE derived by FILDA-2 is in good agreement with limited ground-based observations near the fires. Additionally, FILDA-2 reduces angular dependence in FRP estimates and significantly reduces the "bow-tie" (double-counting) effect in fire detection compared with the AF-I product. The cross-validation of FILDA-2 products from VNP and VJ1 retrievals confirms good consistency in FRP and MCE retrievals globally. FILDA-2 is being implemented by the National Aeronautics and Space Administration (NASA) to generate a new VIIRS data product for fire monitoring, chemical-speciated fire emission estimates, and fire line characterization.**

Index Terms— **Day-night band (DNB), fire detection, fire radiative power (FRP), gas flaring, modify combustion efficiency (MCE), National Oceanic and Atmospheric Administration (NOAA)-20, Suomi-NPP, visible energy fraction (VEF), visible infrared imaging radiometer suite (VIIRS), visible light at night, wildfire.**

Manuscript received 3 September 2022; revised 8 January 2023 and 14 February 2023; accepted 28 February 2023. Date of publication 24 March 2023; date of current version 14 April 2023. This work was supported in part by the Terra, Aqua, and Suomi National Polar-orbiting Partnership (SNPP) Program, National Aeronautics and Space Administration (NASA), under Award 80NNSC21L1976; and in part by the Modeling and Analysis Program, NASA, under Award 80NSSC21K1494. The work of Meng Zhou was supported by the Future Investigators in NASA Earth and Space Science and Technology Program under Grant 80NSSC21K1628. The work of Zhuosen Wang was supported by the Terra, Aqua, and SNPP Program, NASA, under Award 80NSSC22K0199. *(Corresponding authors: Jun Wang; Meng Zhou.)*

Meng Zhou is with the Geo-Informatics and Atmospheric and Environmental Research Laboratory, Iowa Technology Institute, The University of Iowa, Iowa City, IA 52242 USA (e-mail: meng-zhou-1@uiowa.edu).

Jun Wang, Lorena Castro Garcia, and Xi Chen are with the Atmospheric and Environmental Research Laboratory, Department of Chemical and Biochemical Engineering, Iowa Technology Institute, The University of Iowa, Iowa City, IA 52242 USA (e-mail: jun-wang-1@uiowa.edu; lorena-castrogarcia@uiowa.edu; xi-chen-4@uiowa.edu).

Arlindo M. da Silva is with the Global Modeling and Assimilation Office, NASA Goddard Space Flight Center, Greenbelt, MD 20771 USA (e-mail: arlindo.m.dasilva@nasa.gov).

Zhuosen Wang is with the Terrestrial Information Systems Laboratory, NASA Goddard Space Flight Center, Greenbelt, MD 20711 USA, and also with the Earth System Science Interdisciplinary Center, University of Maryland, College Park, MD 20711 USA (e-mail: zhuosen.wang@nasa.gov).

Miguel O. Román is with the Integrated Missions Operation, Leidos Civil Group, Reston, VA 20190 USA (e-mail: miguel.o.roman@leidos.com).

Edward J. Hyer is with the Naval Research Laboratory, Marine Meteorology Division, Monterey, CA 93943 USA (e-mail: edward.hyer@nrlmry.navy.mil).

Steven D. Miller is with the Department of Atmospheric Science and Cooperative Institute for Research in the Atmosphere, Colorado State University, Fort Collins, CO 80523 USA (e-mail: steven.miller@colostate.edu).

This article has supplementary downloadable material available at https://doi.org/10.1109/TGRS.2023.3261664, provided by the authors.

Digital Object Identifier 10.1109/TGRS.2023.3261664

Nomenclature

List of Acronyms

AF	Active fire.
BT	Brightness temperature.
CMG	Climate modeling grid.
DNB	Day/night band.
EPA	Environmental protection agency.
FRP	Fire radiative power.
GEOS-FP	Goddard Earth observing system forward processing.
IGBP	International Geosphere-Biosphere Programme.
I-Band	Imagery resolution band.
LWIR	Long-wave InfraRed.
MAD	Mean absolute difference.
M-Band	Moderate resolution band.
MCE	Modified combustion efficiency.
MDR	Mole density ratio.
MODIS	MODerate resolution Imaging Spectroradiometer.
MWIR	Medium-wave InfraRed.
SAMA	South Atlantic Magnetic Anomaly.
TOA	Top of atmosphere.
VEF	Visible energy fraction.
VIIRS	Visible infrared imaging radiometer suite.
VJ1	VIIRS aboard JPSS-1/NOAA-20.

VLP Visible light power.
VNP VIIRS aboard Suomi-NPP.

List of Parameters

BT_{I4}	BT of the I-band channel 4 (3.74 μm), in K.
BT_{I5}	BT of the I-band channel 5 (11.45 μm), in K.
BT_{M10}	BT of the M-band channel 10 (1.61 μm), in K.
BT_{M13}	BT of the M-band channel 13 (4.05 μm), in K.
DT_{I4}	Dynamical threshold of the I-band channel 4 (3.74 μm), in K.
FRP	Fire radiative power, in W.
L_{DNB}	DNB at sensor radiance, in $Wm^{-2}sr^{-1}$.
L_{DNBb}	Background DNB at sensor radiance, in $Wm^{-2}sr^{-1}$.
L_{M13}	M-band channel 13 (4.05 μm) at sensor radiance, in $Wm^{-2}sr^{-1}\mu m^{-1}$.
L_{M13b}	Background M-band channel 13 (4.05 μm) at sensor radiance, in $Wm^{-2}sr^{-1}\mu m^{-1}$.
$MAD(BT_{I4b})$	Spatial mean absolute deviation of the background BT_{I4}, in K.
$MAD(BT_{I45b})$	Spatial MAD of the background ΔBT_{I45}, in K.
$MAD(BT_{M10b})$	Spatial MAD of the background BT_{M10}, in K.
$MAD(BT_{M13b})$	Spatial MAD of the background BT_{M13}, in K.
MCE	Modified combustion efficiency, unitless.
QF_{I4}	Quality flag of the I-band channel 4 (3.74 μm), unitless.
QF_{I5}	Quality flag of the I-band channel 5 (11.45 μm), unitless.
VEF	Visible energy fraction, unitless.
VLP	Visible light power, in W.
ΔBT_{I45}	BT difference between the I-band channel 4 (3.74 μm) and channel 5 (11.45 μm), in K.
$\overline{BT}_{I4b}$	Spatial mean of the background BT_{I4}, in K.
$\overline{BT}_{M10b}$	Spatial mean of the background BT_{M10}, in K.
$\overline{BT}_{M13b}$	Spatial mean of the background BT_{M13}, in K.
$\overline{\Delta BT}_{I45b}$	Spatial mean of the background ΔBT_{I45}, in K.

I. Introduction

ACTIVE fire detection from *space* offers a valuable tool for monitoring fires in near-real time and studying their impacts on climate change and air quality on a global scale. The identification of active fire locations and estimation of FRP has been a mainstay of existing fire products and have been used to improve estimates of global fire emissions over the past two decades [1], [2], [3], [4], [5], [6], [7], [8], [9], [10], [11], [12], [13]. As reviewed by Polivka et al. [14], while the first detection of fires from space using fire light measured by the Defense Meteorological Satellite Program (DMSP) Operational Linescan System (OLS) instruments occurred in the early 1970s [15], operational active fire detection algorithms have primarily leveraged observations in the MWIR (MWIR at ∼4 μm) spectrum to distinguish the hot anomalies from the cold background and subsequently locate active fires [2], [3], [4], [5], [6], [11], [12], [16], [17], [18], [19], [20].

Current operational detection algorithms employed by the National Oceanic and Atmospheric Administration (NOAA) and the National Aeronautics and Space Administration (NASA) estimate FRP using the MWIR measurement at the pixel level [4], [5], [6], [18], [19]. However, these algorithms are unable to describe the combustion efficiency [21], [22], [23], which is an intrinsic property of a fire and can vary throughout its life regardless of fire size [24]. Combustion efficiency is typically quantified by the mass ratio of carbon emitted as CO_2 to the total carbon emitted as CO_2 and CO, referred to as MCE [24], [25], [26], [27], [28]. While MCE typically ranges from 0.80 to 0.98, a small change of only 0.08 in MCE can result in a factor of up to 20 changes in the emission factor of organic aerosols [27]. Similar changes have been observed for other gas and aerosol species [29], [30], [31]. MCE also significantly impacts the optical properties of the emitted aerosols [32], [33]. Current estimates of smoke aerosol and trace gas emissions vary by a factor of 10 or more depending on the region, time, fuel type, and species of interest [25], [34], [35] in different biomass burning emission inventories, leading to substantial uncertainty in the impact assessment of biomass burning on the Earth. The retrieval of MCE from space can provide much-needed information for constructing a chemical-speciated fire emission inventory and reducing uncertainties.

We present the development and advancement of a nighttime fire detection algorithm that can be used to characterize the FRP and fire MCE based on data from the VIIRS aboard the NOAA/NASA Suomi National Polar-orbiting Partnership (S-NPP) and NOAA-20 satellites. Our work builds upon several recent studies that have combined the visible light measurements from VIIRS DNB with MWIR measurements to either assess the fire combustion efficiency *or* enhance fire detection [6], [14], [18], [24]. In the first generation of the FIre Light Detection Algorithm (FILDA-1), Polivka et al. [14] demonstrated that incorporating the DNB, which is sensitive to radiation in the wavelength range from 0.5 to 0.9 μm, with selected VIIRS moderate resolution bands (M-band, 742 m) at MWIR can detect 30% smaller and cooler fires compared with the operational VIIRS active fire 750-m M-band (AF-M) products. To characterize fire combustion efficiency, Wang et al. [24] introduced a new parameter, i.e., VEF, defined as the ratio of the visible energy emitted by the fire (VLP) to the total FRP, and found that VEF is positively correlated with fire MCE at global, regional, and local scales. As a ratio, VEF is an intensive property, like MCE, and can attain a maximum

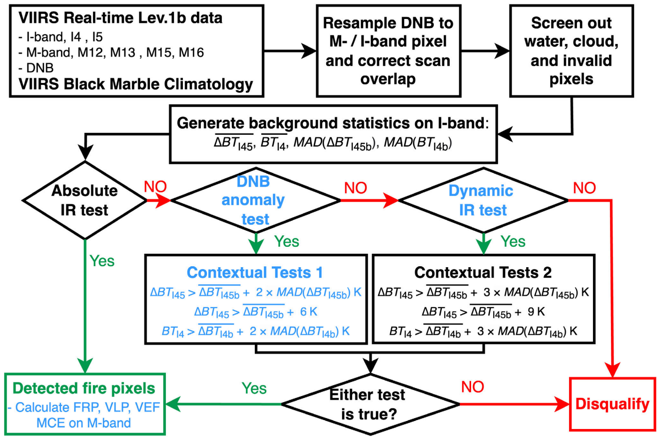

Fig. 1. Flowchart of the FILDA-2 algorithm. The green color indicates the workflow that passes the tests in each step, while the red color indicates the steps that fail the tests. The blue color highlights the improvements of FILDA-2 compared with FILDA. Please refer to the text for further details.

possible value of 1. In terms of the physics of combustion, visible light is intrinsic to flaming combustion, and the larger the visible light intensity, the more flaming occurs, and therefore, the larger the MCE. However, in the work by Wang et al. [24], active fire detection solely utilized M-band MWIR and LWIR (for background temperature estimation) observations.

The new approach integrates the VIIRS DNB, MWIR, and LWIR channels to simultaneously improve fire detection and VEF estimation (indicative of MCE). The algorithm is the second generation of the FILDA-2 and combines the techniques in FILDA-1 [14] with the development of VEF and MCE retrieval algorithm first established in Wang et al. [24]. Furthermore, the FILDA-2 utilizes the VIIRS imagery resolution bands (I-band, 375 m) observations from both the S-NPP and NOAA-20 satellites to improve fire detection. The FILDA-2 algorithm, while conceptually simple, requires surmounting several technical challenges to be practically applied. Section II describes the data used in this study and the necessary techniques for combined utilization of the different VIIRS products. Details of the updates on the FILDA-2 are described in Section III. Section IV provides a comprehensive assessment of the FILDA-2 with the high-resolution data acquired by the Advanced Spaceborne Thermal Emission and Reflection (ASTER) instrument aboard NASA's Terra satellite [36] and other existing data products. Section V summarizes this article.

II. Sensor, Data, and Challenges

Fig. 1 depicts the primary input data and algorithm flow of FILDA-2, which utilizes several data products (Section II-B) from the VIIRS instruments (Section II-A) on the S-NPP and NOAA-20. Although the VIIRS sensors have the same design concepts, they differ in their ways of pixel aggregation for the level-1 radiance data, which poses challenges in aligning DNB, MWIR, and LWIR measurements to the same ground footprint (Section II-C).

A. VIIRS Sensor

VIIRS is the primary imager aboard S-NPP and NOAA's polar-orbiting joint polar satellite system (JPSS) series of satellites for the next two to three decades [37], [38], [39], [40], [41]. It is a 22-band scanning radiometer with a nominal spatial resolution of 375 m in the five "imagery bands" I-bands, 750 m in 16 "moderate resolution" M-bands, and the DNB [42], [43]. VIIRS differs from its predecessors, such as the advanced very-high-resolution radiometer (AVHRR) [44] and the MODIS [45] in several ways that are significant for fire detection applications: 1) due to cross-track onboard aggregation of detectors, the pixel size growth factor from the nadir to the edge of the scan (EOS) is about 4 [38], [41], much smaller than the 8–10 growth factor for MODIS [46], [47]; 2) the VIIRS DNB can measure visible light intensity in a range of seven orders of magnitude [42], including levels down to the equivalent of a quarter moon phase or less, orders of magnitude lower than conventional visible bands; and 3) measurements of shortwave radiation at wavelengths of 0.865 (M07), 1.24 (M08), 1.61 (M10), 2.25 (M11), 3.74 (I4), 3.70 (M12), and 4.05 μm (M13) are available at night, whereas MODIS only has a 3.96 μm MWIR channel for fire detection at night.

Currently, two VIIRS sensors are flown, respectively, on the S-NPP (hereafter VNP) and the NOAA-20 (previously named joint polar satellite system-1 or JPSS01, referred to here as VJ1) satellites [40]. VNP was the first VIIRS sensor launched in 2011 and has a sun-synchronous orbit that synoptically observes the Earth at roughly 1:30 P.M. local time in its ascending node, and a corresponding descending node observes the Earth at 1:30 A.M. used for this research. VJ1 was launched in late 2017 and operates on the same orbital plane [48] as VNP, but the overpassing time is 50 min ahead (00:40 A.M. and 00:40 P.M., respectively). Together, these sensors allow important overlap in observational coverage and consequently provide the science and application communities with a daily global near-nadir view of the Earth within a one-hour time window at the complementary view and illumination geometries. At the time of this writing, there are plans to launch JPSS-2 (to become NOAA-21 once operational) in November 2022, which will be inserted into the same orbital plane as S-NPP and NOAA-20, and thus, provide multiple observations centered around the 1:30 A.M./P.M. crossing times [49].

B. Data and Data Processing

1) FILDA-2 Input Dataset: Table I summarizes the VIIRS bands used in FILDA-2. The primary input datasets for FILDA-2 are: 1) VIIRS level-1B calibrated DNB radiance data (VNP02DNB [50] and VJ102DNB [51]) and the DNB geolocation product (VNP03DNB [52] and VJ103DNB [53]), used for fire identification and VEF and MCE derivation; 2) VIIRS level-1B calibrated M-band radiance data (VNP02MOD [54] and VJ102MOD [55]) and the geolocation product (VNP03MOD [56] and VJ103MOD [56]), used for the cloud masking and FRP, VEF, and MCE estimation; and 3) VIIRS level-1B calibrated I-band radiance data (VNP02IMG [57] and VJ102IMG [58]) and the I-band geolocation product (VNP03IMG [59] and VJ103IMG [60]), used for fire identification. All the VIIRS products can be obtained through the NASA level-1 and atmosphere archive and distribution system (LAADS, https://ladsweb.modaps.eosdis.nasa.gov/). While the 3.74 μm (I4) band is the

TABLE I
CHARACTERISTICS OF THE VIIRS BANDS USED IN THE FILDA-2

Band number/Gain	Central Wavelength (μm)	Nadir resolution along-track $\times$ cross-track (m^2)	Saturation Vaule[1]	Primary application in FILDA-2
DNB, multiple	0.5-0.9	742 $\times$ 742	400	Fire detection, VEF calculation
M10, single	1.61	742 $\times$ 766	85.48	Fire detection
M12, single	3.70	742 $\times$ 766	368	Cloud mask
M13, dual	4.05	742 $\times$ 766	683	Fire detection, FRP calculation
M15, dual	10.78	742 $\times$ 766	381	Cloud mask
M16, single	12.01	742 $\times$ 766	382	Cloud mask
I4, single	3.74	371 $\times$ 387	367	Cloud mask, Fire detection
I5, single	11.45	371 $\times$ 387	380	Cloud mask, Fire detection

[1] The unit is $\mathrm{Wm^{-2}sr^{-1}}$ for DNB, $\mathrm{Wm^{-2}sr^{-1}\mu m^{-1}}$ for M10, and K for M12-M16 and I4-I5 [65].

main channel for fire identification in FILDA-2, previous research [6] suggested that two primary types of anomalies can affect its application on fire detection: 1) saturation due to its single-gain channel nature [61] and 2) SAMA [62], [63]. The SAMA also affects the observational quality of the VIIRS DNB [64]. Section III-C1 addresses the saturation of the I4-band and Section III-C4 addresses the SAMA issues for fire detection.

Other ancillary datasets and the respective preprocessing steps used prior to the retrieval of fire characteristics at the pixel level are listed as follows.

1) The standard S-NPP VIIRS black marble nighttime light product (VNP46A1) [66] is used for generating a global surface light climatology. VNP46A1 contains daily, TOA, at-sensor nighttime radiance gridded to 15 arc-second linear latitude/longitude grid. We fit three months of DNB radiance data of each pixel of VNP46A1 into a gamma distribution to derive the shape parameter α and the rate parameter β, under the assumption that the DNB radiance for a specific location obeys a gamma distribution. These two parameters form the historical nighttime light climatology used later to identify visible light anomalies and select the fire candidates (Section III-C). VNP46A1 is the at-sensor radiance product without any corrections. The future improvement includes exploring the VNP46A2 to parameterize the surface light climatology. The VNP46A2 data product contains the daily at-sensor TOA nighttime DNB radiance at 15 arc-second resolution after correction of Lunar, cloud, terrain, atmospheric, snow, airglow, stray light, and seasonal canopy effects, and intelligent gap filling [67].
2) We use temperature data from the GEOS-FP forecast product [68] as part of the surface flux diagnostics (tavg1_2d_flx_Nx) to aid in the processing of an internal nighttime cloud mask (Section III-B). The tavg1_2d_flx_Nx dataset has a spatial resolution of 0.25° $\times$ 0.375° and a temporal resolution of 1 h. Surface temperatures are first linearly interpolated to the VIIRS overpass time and then interpolated bilinearly to match the VIIRS geolocation.
3) MODIS monthly normalized difference vegetation index (NDVI, MOD13C2, and MYD13C2) [69], [70] is used to derive the multiyear monthly NDVI climatology, which is used later in the internal cloud detection (Section III-B).
4) The MODIS Terra and Aqua combined land cover product (MCD12Q1) [71], [72] is used to specify the land surface type of each fire pixel, as needed by the fire emission modeling community. The MCD12Q1 contains 17 land categorizations defined by IGBP, It is worth noting that peatland is not considered one of the IGBP land surface types.
5) A peatland database [73] is included to specifically designate peatland fire pixels. This is necessary because the peatland fires have distinctly different emission factors compared with fires on other land types [74], [75], [76]. To accelerate the speed of the algorithm, we rasterize the shapefile in the database into a 0.005° $\times$ 0.005° raster image, as shown in Fig. 2. It is also worth noting that the peatland database is not mutually exclusive with the MCD12Q1. The provided information is an additional *peatland* flag to identify the presence of peatland within the fire pixels.
6) A global gas flaring dataset (Fig. 2) is used to identify gas flaring pixels detected by FILDA-2 [77]. The dataset is originally provided in point source format, which was rasterized into a 0.005° $\times$ 0.005° raster image using the same process as for the peatland dataset.

2) Validation Dataset: Table II lists the datasets used in validating the FILDA-2 fire detection and fire parameters estimation, and they are listed as follows.

1) The band-10 (8.3 μm) radiance data from the ASTER is used to verify the fire detection made by FILDA-2. With a spatial resolution of approximately 90 m, the ASTER band-10 is capable of detecting hot spots during nighttime. To the best of our knowledge, it is the only high-resolution sensor that has routine observations at night and can provide the co-occurred subhundred-meter evidence of a fire incident for the validation of the fire detection algorithms. Due to its co-occurring and high-resolution nature, it has been widely used as a reference for fire detection validation in previous studies [41], [78], [79].
2) The operational VIIRS 750 m AF-M product and 375-m I-band active fire detection (AF-I) product are used as references for comparison of fire detection and FRP estimation of FILDA-2. Currently, AF-M and AF-I products are generated by NASA and NOAA, under identical physical principles, simultaneously, and independently. The AF-M and AF-I products used for comparison are

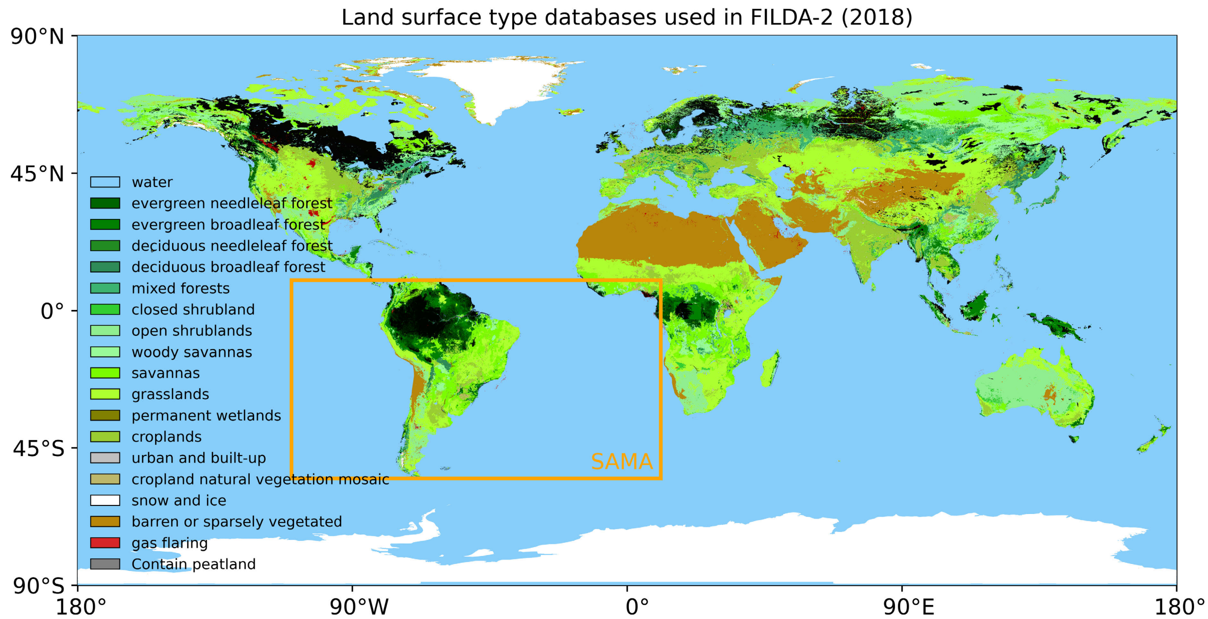

Fig. 2. Illustration of land surface types used in FILDA-2 for the year 2018, including IGBP, Peatland, and gas flaring databases from multiple sources. The IGBP product used is MODIS Terra and Aqua combined land cover product (MCD12Q1) and updated for each year; the peatland dataset is a static dataset, sourced from the PEATMAP at the University of Leeds, Leeds, U.K., and has been rasterized to a resolution of 0.005°; the gas flaring dataset has a resolution of 0.005° and is also updated annually. The region affected by SAMA is defined in Section III-C4. See text for details.

TABLE II
DATASETS USED IN THE VERIFICATION

Dataset	Content of verification	Spatial resolution	Time	Domain
ASTER band 10 radiance	Fire detection	90 m	Nov. 2019 to Jan. 2020	Australia
VNP14	Fire detection, FRP estimation	750 m	Aug. 2019 to Jul. 2020	Global
VNP14IMG	Fire detection, FRP estimation	375 m	Aug. 2019 to Jul. 2020	Global
EPA CO and NO_2 measurement	MCE estimation	Point source	06 to 26 Sept. 2020	Los Angeles

from NASA LAADS. The AF-M (VNP14) [5] product uses the spectral contrast of 4.05 (M13) and 10.78 μm (M15) to provide fire locations and FRP estimates. The AF-I product (VNP14IMG) [6] utilizes the 3.74 (I4) and 11.45 μm (I5) to provide fire location. Since the I4-band is a single-gain band originally designed for Earth imaging and cloud studies, it can be easily saturated when the kinetic temperature of fire exceeds 367 K. Consequently, I-band observations are only used for detecting fire pixels, while the FRP in each I-band fire pixel is calculated based on the collocated M-band observations. Although at the detection level, VIIRS I-band products can provide more fire pixels detected with a higher spatial resolution (including more detection than Terra/Aqua MODIS products, combined) [6], it lacks the ability to distinguish the variations of FRP between I-band fire pixels within in the same M-band pixel.

3) Measurements of CO and NO_2 from the U.S. EPA, Washington, DC, USA, were used to validate the MCE derived in this work.

C. Configuration of DNB and M-Band on VIIRS and Difference Between VNP and VJ1 DNB

Due to differences in pixel resolutions and aggregation schemes, mismatches in spatial coverage or differences in footprint size may occur among I-band, M-band, and DNB pixels that contain the same fire on the ground [24]. These differences are critical to a fire detection algorithm that requires multispectral data for the exact same location or footprint on the ground. In brief, while the DNB has the same along-track extent on the focal plane assembly (FPA) as all the other M-band or I-band sensors, it has 250 subpixel charge-coupled device (CCD) detectors in the cross-track direction and 672 subpixel detectors along the track direction. However, the M-band and I-band sensors have only 16 and 32 along-track 1-D detectors, respectively. For the VNP sensor, the sampling time of the I-band and M-band in the cross-track direction is 44.1295 and 88.259 μs, respectively, while for DNB it is only 3.8373 μs. These differences enable VNP DNB to have a much finer resolution of 18 $\times$ 11 m at the nadir and 38 $\times$ 69 m at the end of the swath for the footprint of each detector providing a larger degree of freedom for VNP DNB through the aggregation of these detector data to formulate the level-1B pixel data that sustain a nearly constant pixel size of 742 m throughout the swath (aggregation option 32, Opt32) [80]. VNP DNB has a nominal scan angle of $\pm$56.06°, which covers approximately the same area as the M-band and I-band with a swath width of 3060 km across the track. The VNP DNB sensor data record (SDR) product has a total of 4064 Earth view (EV) samples/pixels per scan line, while the EV sample number is 3200 for the M-band and is doubled

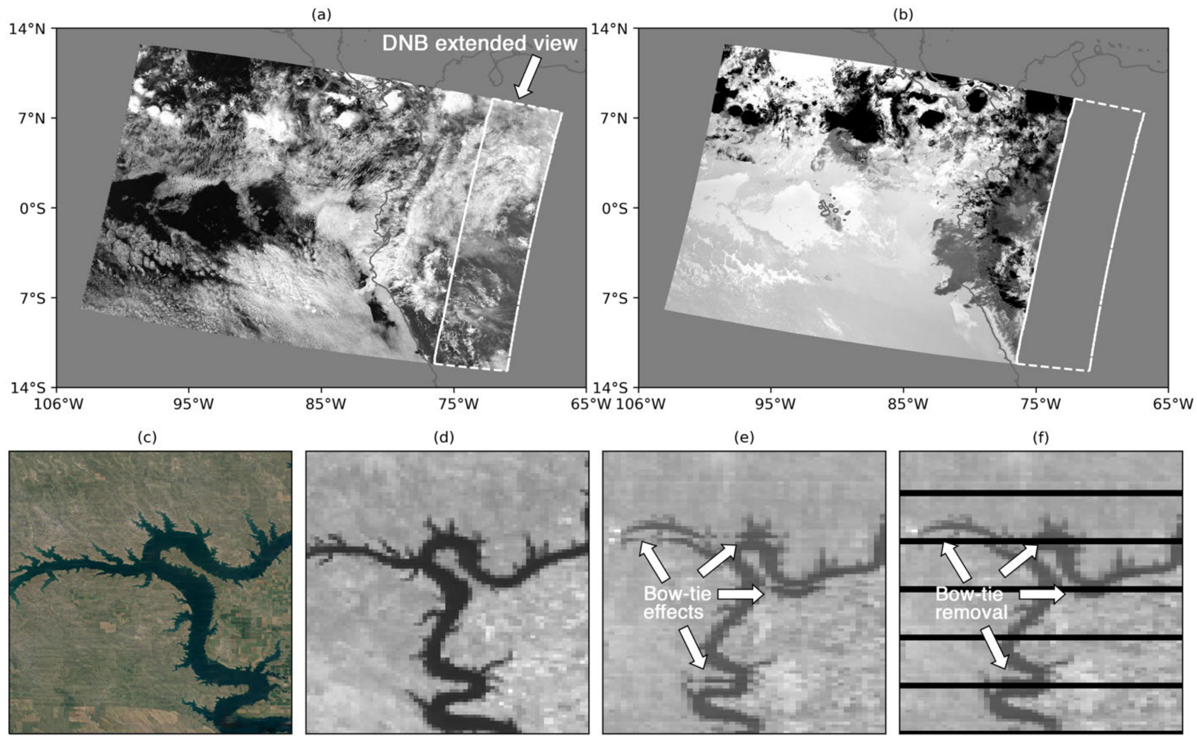

Fig. 3. Illustrations of VJ1 DNB nonlinearity in the onboard aggregation of detector footprints to form level-1B pixels. (a) VJ1 DNB nighttime TOA reflectance image on August 14, 2019. (b) VJ1 M13 (4.05 μm) BT image, the same observation time as (a). (c) Google Earth image of Missouri River in South Dakota (SD). (d) VJ1 DNB image of Missouri River in SD, nadir view (Aggregation mode 1, Zone 31). (e) Same as (d), but for aggregation Zone 63 (at the edge of the scan) where the bow-tie effect often can be found due to the use of the pixel aggregation mode 21 in the VJ1 design. (f) Same as (e) with the removal of bow-tie pixels (remove as denoted as the black stripes). See text for details.

to 6400 for the I-band. The VNP DNB SDR product has nearly no bow-tie effect or swath overlap due to the superior on-board aggregation [14], [24].

VJ1 DNB differs from VNP DNB in the method that is used to aggregate the radiances from individual subpixel CCD detectors to calculate the radiance on DNB resolution, which affects the data handling for each sensor in the FILDA-2. Although both DNB sensors have the same design, the VJ1 DNB showed high nonlinearity in the radiometric response for high gain (nighttime illumination levels) focal plane arrays during the prelaunch radiometric calibration stage [81]. This nonlinearity is specific to certain detectors and depends on the aggregation mode and can be especially pronounced at high scan angles [82]. To mitigate this issue, the JPSS Data Working Group proposed two new aggregation options: aggregation option 21 (Op21, which holds aggregation mode 21 constant out to scan edge) and aggregation option 21/26 (Op21/26). Op21 was ultimately chosen for VJ1 DNB due to its better radiometric performance [83]. The major observational differences between the Op21 (used for VJ1 DNB) and Op32 (used for VNP DNB) are: 1) VJ1 only has a nearly constant pixel size within $\pm 49.1^{\circ}$ of the scan angle. Beyond this range, the pixel size grows with scan angles due to the aggregation of more subpixels compared WITH Op32 and 2) the EV frame for VJ1 ends at a scan angle of $\pm 60.5^{\circ}$, which allows for the aggregation of more detectors at high scan angles. These differences result in a wider swath of $\sim$3650 km and a slightly larger increase in pixel size at the end of the scan for VJ1 DNB. Consequently, as shown in Fig. 3(a) and (b), there is a $\sim$600-km extent of EV samples in the VJ1 DNB swath compared with those in the VNP DNB and other VJ1 bands. The VJ1 DNB SDR product also exhibits a bow-tie effect and overlaps between scans, as shown in Fig. 3(e), which are significantly greater than those found in VNP DNB.

III. FILDA-2 Algorithm

Three steps are taken to process each VIIRS data file (typically every 6 min, as shown in Fig. 3). The first step (shown in the first row of Fig. 1) involves processing the data to resample DNB radiance to the footprint of each VIIRS M- and I-bands pixels (denoted as $L_{\mathrm{DNB-M}}$ and $L_{\mathrm{DNB-I}}$, respectively) and removing pixels affected by the bow-tie effect, water, and twilight. The second step (shown in middle part of Fig. 1) integrates the $L_{\mathrm{DNB-I}}$ data, I-band channel-4 3.74 μm BT ($\mathrm{BT_{I4}}$), and I-band channel-5 11.45 μm BT ($\mathrm{BT_{I5}}$) for comprehensive fire detection. The final step retrieves fire parameters (FRP, VEF, and MCE) at M-band resolution for each fire pixel utilizing the $L_{\mathrm{DNB-M}}$ and M-band channel-13 4.05 μm radiance (L_{M13}). This section details the technical steps of the algorithm.

A. Collocation and Alignment of M-Band and I-Band Pixels With DNB

The first step in the FILDA-2 is to bring the VIIRS DNB, I-band, and M-band data into one consistent spatial

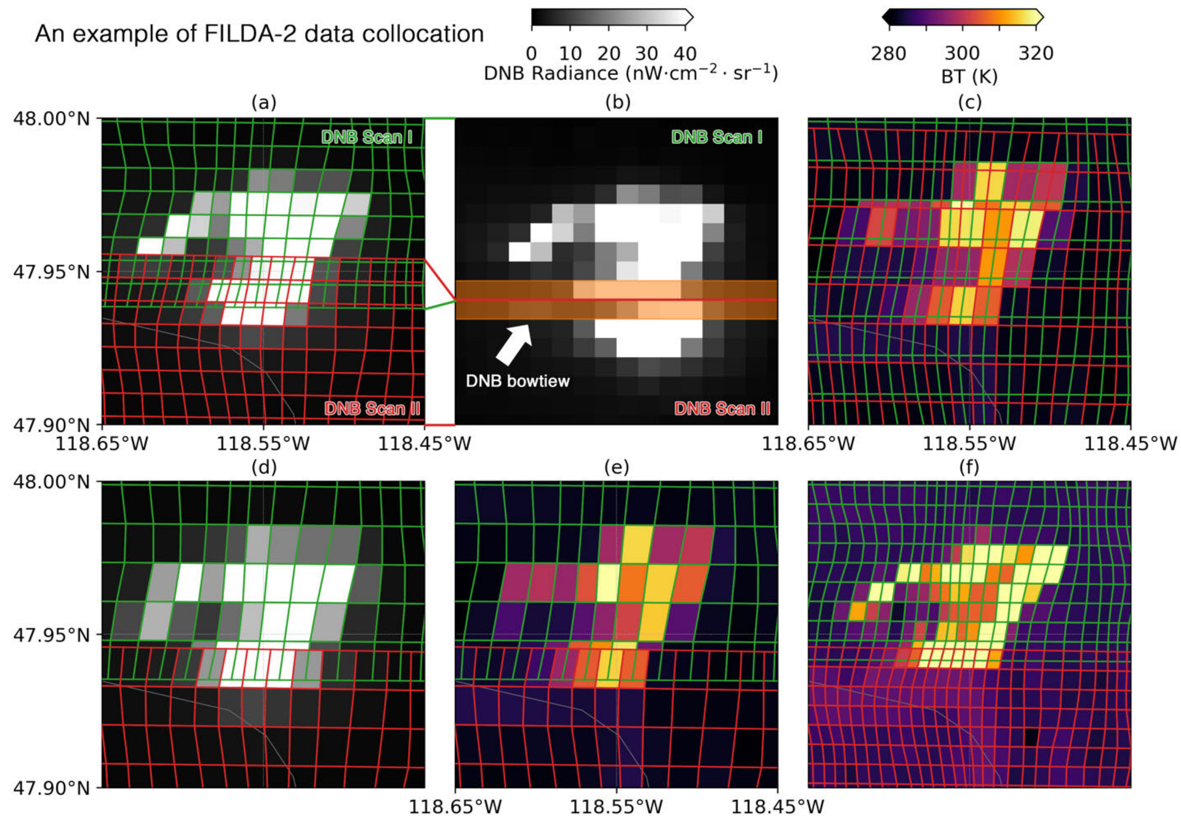

Fig. 4. Example of DNB, I-band, and M-band collocation and homogenization. (a) VJ1 DNB observation on August 8, 2019, in its native resolution. (b) Same as (a) but without projection on the Eart's surface. (c) Same as (a) but for M13 (4.05 μm) BT. (d) Resampled VJ1 DNB observation in M-band resolution with the removal of bow-tie-affected pixels. (e) M13 BT with the removal of bow-tie-affected pixels. (f) VJ1 3.74 μm I-band BT with the removal of bow-tie-affected pixel. In (a) and (b), the bright pixels were fire affected area, while the dark pixels are the background area. The green and red mesh grids are the pixel footprints of two consecutive scan blocks. See text for details.

resolution. While this process is relatively simple for the I-band and M-band, as one M-band pixel holds four I-band pixels, collocating the DNB pixel with the M-band and I-band pixels is more complex. To address this, a fast collocation algorithm was developed by Wang et al. [24] to resample the VNP DNB radiance to the M-band footprint. It includes the following steps: 1) segregate the M-band data into different DNB aggregation zone; 2) project the M-band and DNB footprints onto the Earth's surface using Albers's equal-area projection; 3) detect the DNB pixels that overlap with a given M-band footprint; 4) calculate the areal weights for each identified DNB pixel in 3); and 5) resample the DNB radiance to match the M-band resolution.

However, this method is dependent on the aggregation schemes of the DNB and M-band and may not be suitable for future VIIRS sensors with different aggregation options. To create a more general resampling method that can be applied to any VIIRS sensor and handle any aggregation mode, we developed a new method that calculates the resampling coefficients for each I-band and M-band pixel in a cross-track scan independently. This avoids the need to consider the varying aggregation pattern of each VIIRS sensor and allows for continuity in the fire data product across future VJ2, VJ3, and VJ4 sensors. To derive the resampling coefficients, we carefully selected a VIIRS scan near the equator where projection deformation, as represented by Tissot's indicatrix [84], was minimized. The new method entails the following steps: first, for each I-band or M-band footprint (target footprint), we used a $0.05^{\circ} \times 0.05^{\circ}$ spatial window to identify the DNB footprints (candidate DNB footprints) that potentially overlap with the target I-band or M-band footprint in the geographic coordinate system. Second, we projected the target footprint together and candidate DNB footprints onto the Earth's surface using Albers's equal-area projection with projection parameters that minimized Tissot's indicatrix. Third, we applied the Weiler–Atherton clipping algorithm [85] to determine the intersection between the candidate DNB footprint and the target footprint and calculate the overlap areas. Finally, we used the Shoelace formula [86] to calculate the area of the target footprint and determine the resampling weights for each I-band and M-band footprint. Redundant overlapping pixels caused by the bow-tie effect were removed, similar to the method proposed by Wang et al. [24]. This transformation only needs to be applied once to a representative sample scan, and the results, including indices and weights of the DNB pixels, for each I-band and M-band footprint along the scan line are saved in a lookup table [24]. The lookup table allows us to efficiently map all DNB pixels in each granule onto the M-band and I-band in the same granule for the FILDA-2 algorithm (Fig. 4).

B. Removal of Cloud, Water, and Twilight Pixels

In FILDA-2, cloudy pixels are identified on both M-band and I-band resolutions through two sets of IR tests on the

M-band and I-band, separately. The final cloud mask used in the FILDA-2 is generated by merging the M-band and I-band cloud masks. To be conservative in identifying clear pixels, the two masks are combined using the Boolean union operation, meaning that if an M-band pixel is detected as cloudy, all the collocated I-band pixels will also be marked as cloudy. The M-band cloud mask is created using three BT tests on 3.70 (M12), 10.78 (M15), and 12.01 (M16) μm channels, respectively. First, if the 10.78 μm BT (BT_{M15}) for a given pixel is lower than the corresponding surface temperature estimated from GEOS-FP by 10 K or more, then that pixel is considered as a cloudy pixel. Second, if the BT difference between 10.78 and 3.70 μm is positive over the vegetated surface (with monthly mean climatology of NDVI > 0.25), it is indicative of nighttime low-level water cloud due to the lower cloud emissivity at 3.70 μm. Third, the BT difference test between 10.78 and 12.01 μm is used to detect the cirrus clouds. The cloud mask algorithm for I-band resolution goes through two BT threshold tests, respectively, at BT_{I4} and BT_{I5}; pixels whose BT_{I4} and BT_{I5} values are smaller than 295 K and 265 K, respectively, will be identified as cloudy pixels. After cloudy pixels are removed, the remaining pixels are further filtered to remove water pixels (using pixel *land_water_mask* within VIIRS level-1B geolocation data) and twilight pixels (solar zenith angle is less than 100°) before the fire detection process.

C. Identification of the Fire Pixel

The process of identifying the fire pixels from cloud-free pixels consists of two consecutive steps on the top level: the absolute and dynamic tests to identify fire pixel candidates, and the contextual test which exploits dynamic thresholds to screen the fire pixels.

1) Absolute Test: Pixels that clearly show energy signatures indicative of a fire or thermal anomaly are identified first, following the methods used by the AF-I algorithm [6]. If a pixel satisfies any of the following criteria, it will be labeled as a fire pixel:

$$\mathrm{BT_{I4}} > 320\ \mathrm{K}\ \text{and}\ \mathrm{QF_{I4}} = 0 \tag{1}$$

or

$$\mathrm{BT_{I4}} = 367\ \mathrm{K}\ \text{and}\ \mathrm{QF_{I4}} = 4 \tag{2}$$

or

$$\Delta\mathrm{BT_{I45}} < 0\ \mathrm{K}\ \text{and}\ \mathrm{BT_{I5}} > 310\ \mathrm{K}\ \text{and}\ \mathrm{QF_{I5}} = 0 \tag{3}$$

or

$$\mathrm{BT_{I4}} = 208\ \mathrm{K}\ \text{and}\ \mathrm{BT_{I5}} > 335\mathrm{K}\ \text{and}\ \mathrm{QF_{I5}} = 0 \tag{4}$$

where ΔBT_{I45} is the BT difference between BT_{I4} and BT_{I5} and QF_{I4} and QF_{I5} are the pixel quality flags of channel I4 and I5, respectively. A zero value of those quality flags guarantees an unsaturated status of the observation on the corresponding bands, while a value of 4 indicates the saturation status. Equations (2)–(4) enable FILDA-2 to include the high temperature I4-band saturated pixels as absolute fire pixels [6]. FILDA-2 calculates the fire parameters for the absolute fire pixels without any additional down-selection. After the absolute test, FILDA-2: 1) applies the dynamic threshold test to the remaining cloud-free pixels to select the potential fire candidate pixels and 2) applies the contextual test to ultimately identify the fire pixels.

2) Dynamical Threshold Test With a Constraint of DNB: The selection of fire pixel candidates entails two stages. First, nighttime visible light anomalies are picked out through the probability test on the $L_{\mathrm{DNB-I}}$ obtained in Section III-A, given by

$$p_{\mathrm{DNB}} = 1 - F(L_{\mathrm{DNB-I}}, \alpha, \beta) < 1\% \tag{5}$$

where $F(L_{\mathrm{DNB-I}}, \alpha, \beta)$ is the cumulative distribution function of a Gamma distribution. The fitting parameters used are the shape parameters α and the rate parameter β derived, as described in Section II-B. Pixels whose $L_{\mathrm{DNB-I}}$ values are significantly greater than the climatology (with $p_{\mathrm{DNB}} < 1\%$) would be flagged as visible light anomalies. For these pixels, a fire candidate is determined according to

$$\mathrm{BT_{I4}} > \mathrm{DT_{I4}}\ \text{and}\ \Delta BT_{\mathrm{I45}} > 3 \times \mathrm{MAD}(\Delta BT_{\mathrm{I45}}) \tag{6}$$

where DT_{I4} is the dynamical threshold (DT) determined for each visible light intensity anomaly. It is the mean value of BT_{I4} in a 501 × 501 pixel area (equivalent to 187 × 187 km^2) centered at a fire pixel candidate, including only "clean background" pixels, that is, after exclusion of cloudy, water, and absolute fire pixels. The $\mathrm{MAD}(\Delta BT_{I45})$ is the spatial MAD of the ΔBT_{I45}. Visible light anomaly pixels that satisfied (6) are considered as the candidate fire pixels and included in subsequent contextual tests. Compared with the operational VIIRS AF-I product that requires $BT_{I4} > 295$ K and $\Delta BT_{I45} > 10$ K [6], both of these selection criteria are relaxed taking advantage of the visible light information that is a strong indicator of fire at night. While this step is sufficient for fire detection in the rural-mountain and intermountain regions where the existence of artificial light is minimal and further removed based on the climatology of artificial light locations, it can be less robust in the city areas where the light may not arise from the same source of thermal anomaly seen from the infrared bands. In these cases, the thermal anomalies around the stable surface light sources will primarily be detected based on the test in IR bands.

For pixels that are not flagged as anomalous by the DNB probability test, a more stringent test on the IR band is applied, given by

$$\mathrm{BT_{I4}} > 295\ \mathrm{K}\ \text{and}\ \Delta\mathrm{BT_{I45}} > 10\ \mathrm{K}. \tag{7}$$

Only pixels that pass the dynamical threshold test (5), (6), or (7) are classified as fire pixel candidates and proceed onward to the battery of contextual tests.

3) Contextual Test: The contextual test implemented in FILDA-2 is to confirm the ultimate status for the potential fire pixel candidates identified in Section III-C2. In concept, this step consists of a set of probability tests customized for each fire pixel candidate. The statistics used in forming those tests are generated from the "clean background" pixels adjacent to the fire pixel candidate using a dynamically assigned window.

To minimize the impact of the thermal anomalies on the background statistics, we further remove the pixels that have a high probability to be a fire pixel from the clean background as described earlier since they may potentially increase the value of the background temperature, using the following criterion:

$$\mathrm{BT_{I4}} > 300\ \mathrm{K\ and}\ \Delta\mathrm{BT_{I45}} > 10\ \mathrm{K}. \quad (8)$$

The parameters to be retrieved for the contextual test include the spatial mean of the background $\mathrm{BT_{I4}}$ ($\overline{\mathrm{BT}}_{\mathrm{I4b}}$), the spatial mean of the background $\Delta\mathrm{BT_{I45}}$ ($\overline{\Delta\mathrm{BT}}_{\mathrm{I45b}}$), the spatial MAD of the background $\mathrm{BT_{I4}}$ ($\mathrm{MAD(BT_{I4b})}$), and the spatial MAD of the background $\Delta\mathrm{BT_{I45}}$ ($\mathrm{MAD}(\Delta\mathrm{BT_{I45b}})$). For the I-band, the size of the spatial sampling window, centered at each fire pixel candidate, ranges dynamically from 11×11 ($4 \times 4\ \mathrm{km}^2$) up to 51×51 pixels ($20 \times 20\ \mathrm{km}^2$) until at least 25% or 30% usable pixels are encountered. These customized statistics are used to form the contextual criteria applied to each fire candidate for the confirmation of its ultimate status based on the N-σ rule, given by

$$\Delta\mathrm{BT_{I45}} > \overline{\Delta BT}_{\mathrm{I45b}} + \gamma \times \mathrm{MAD}(\Delta\mathrm{BT_{I45b}}) \quad (9)$$

$$\Delta\mathrm{BT_{I45}} > \overline{\Delta BT}_{\mathrm{I45b}} + \delta \quad (10)$$

$$\mathrm{BT_{I4}} > \overline{\Delta BT}_{\mathrm{I4b}} + \epsilon \times \mathrm{MAD(BT_{I4b})}. \quad (11)$$

The values of γ, δ, and ϵ in the tests are determined upon the score of its DNB probability test (p_{DNB}) in Section III-C2. If $p_{\mathrm{DNB}} < 0.5\%$ (rare than a 2.5-sigma event), the following values are used: $\gamma = 2.5, \sigma = 7.5$, and $\epsilon = 2.5$; otherwise, rigid criteria are applied as $\gamma = 3$, $\sigma = 9$, and $\epsilon = 3$. The contextual test is essentially a set of hypothesis tests with statistics. Because the DNB has been shown to be effective for detecting smaller and cooler fires, thresholds for pixels that pass the DNB tests are less strict.

4) Filtering the SAMA False Alerts: The SAMA is a known source of false fire detections in the VIIRS data, to exclude the false alters caused by the SAMA. Following [6] and [63], the region extending from 10°N to 55°S and −110°W to 11°E is defined as the region of SAMA influence in FILDA-2. Fires detected within this region are then subjected to cross-checks on the collocated 1.61- (M10) and 4.05 μm (M13) BT. Using the size of the same window that matches the contextual test (for absolute fire, a 25×25 window is preassigned), the background BT mean of M10 channel ($\overline{\mathrm{BT}}_{\mathrm{M10b}}$) and M13 channel ($\overline{\mathrm{BT}}_{\mathrm{M13b}}$), and corresponding $\mathrm{MAD(BT_{M10b})}$ and $\mathrm{MAD(BT_{M13b})}$ are used to filter out false alerts caused by the SAMA, given by

$$\mathrm{BT_{M10}} > \overline{\mathrm{BT}}_{\mathrm{M10b}} + 3 \times \mathrm{MAD(BT_{M10b})} \quad (12)$$

$$\mathrm{BT_{M13}} > \overline{\mathrm{BT}}_{\mathrm{M13b}} + 3 \times \mathrm{MAD(BT_{M10b})}. \quad (13)$$

Fire pixels that fail these tests are downgraded to a clean pixel and flagged as *SAMA-affected*.

D. Retrieval of Fire Parameters

Since there is possible saturation in I4-band observation, FILDA-2 calculates the FRP, VLP, VEF, and MCE on the M-band. For an M-band fire pixel, its FRP is distributed equally among the I-band fire pixels contained within that M-band pixel. The FRP is calculated for an M-band fire pixel by the following:

$$\mathrm{FRP} = \frac{A\sigma(L_{\mathrm{M13}} - L_{\mathrm{M13b}})}{C} \quad (14)$$

where A is the pixel area (in unit of m^2), σ is the Stefan–Boltzmann constant, C is a sensor and channel dependent fitting parameter [5], [87] (for VIIRS M13 channel, $C = 2.88 \times 10^{-9}\mathrm{Wm^{-2}sr^{-1}}\mu\mathrm{m^{-1}K^{-4}}$). L_{M13} is the M13 radiance of a fire pixel, and L_{M13b} is the mean of the background M13 radiance sampled by the same spatial dynamical window used in Section III-C3.

As a parameter, the VLP value for each fire pixel is calculated via a modification of Wang et al. [24]

$$\mathrm{VLP} = \pi A(L_{\mathrm{DNB}} - L_{\mathrm{DNBb}}) \quad (15)$$

where L_{DNB} is the DNB radiance for the fire pixels, and L_{DNBb} is its background counterpart. It is the mean of the 1% minimum clean and water-free DNB radiance for the entire granule aiming to offset the impact of the moonlight.

VEF is defined as the ratio of the VLP and the FRP, given by

$$\mathrm{VEF} = \frac{\mathrm{VLP}}{\mathrm{FRP}}. \quad (16)$$

MCE calculation follows Wang et al. [24] with slight modification. In the FILDA-2, the intercept of the regression is fixed as 1, considering that the upper bound of MCE is 1. This leads to the slope coefficient changing from 0.016 to 0.017

$$\mathrm{MCE} = 0.017\ \ln\mathrm{VEF} + 1. \quad (17)$$

It is worth noting that the visible light power detected over city regions or stable light sources is less reliable to be used in the calculation of fire combustion status. These pixels are flagged as *city* pixels in the FILDA-2 product. There is also evidence that light emissions in high latitudes, such as airglow and aurora borealis radiance, can reach values higher than 60 $\mathrm{nWcm^{-2}sr^{-1}}$ in DNB observation [67]. Fires under aurora borealis conditions are likely rare because they both are ephemeral phenomena; if in the cases they do coincidentally occur, positive biases will be brought into the estimation of the VLP, VEF, and consequently the MCE. Currently, there is no effective approach in FILDA-2 to recognize airglow and aurora, but this will be a future refinement.

IV. Results

The products generated from FILDA-2 science compute facility (SCF) are available on the website of Atmospheric and Environmental Research (AER) Laboratory, The University of Iowa, Iowa City, IA, USA, via (http://esmc.uiowa.edu:3838/fires_detection/). To demonstrate the performance of the new developments, we selected several typical wildfire events based on the size of the fire and the availability of coincident ASTER overpasses. Global comparisons of the FILDA-2 products with the standard VIIRS AF-M and AF-I products are also presented in Sections IV-A–IV-E.

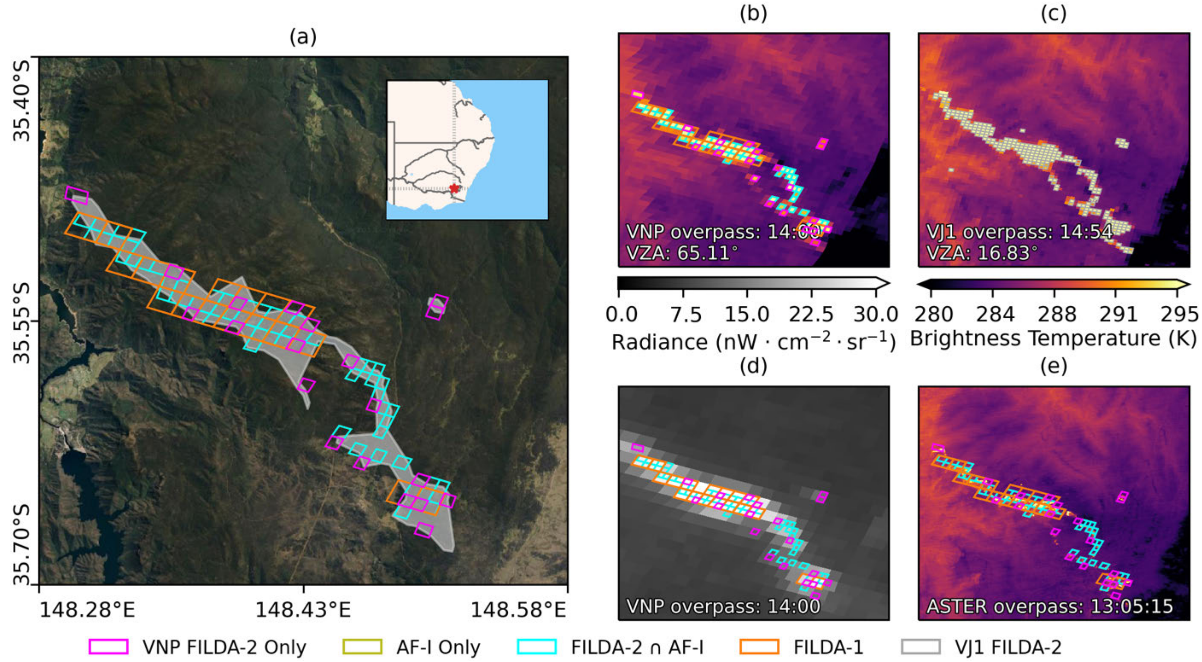

Fig. 5. Multiband and multisensor view of the black summer bushfire on January 8, 2020, by VIIRS and ASTER. (a) Google image of the fire event. (b) VNP I-band 3.74 μm BT at 14:00 UTC; the averaged view zenith angle for this scene is ~65.1°. (c) VJ1 I-band 3.74 μm BT at 14:54 UTC with a view zenith angle of 16.8°. (d) Same as (b) but for resampled DNB observation at M-band resolution. (e) ASTER 8.3 μm image overpass at 13:05 UTC. The boxes on the images indicate the fire pixel footprints color-coded according to their corresponding detection algorithms. FILDA-2 VJ1 detection in (c) is displayed as light-gray-shaded areas in (a). The resolution of FILDA-2 (VNP and VJ1) and AF-I detection are 375 m, and for FILDA-1 it is 750 m. The orange circle indicates an isolated fire event that is ~5 km away from the fire front. See text for details.

A. 2019/2020 Black Summer Bushfire Season

The 2019/2020 black summer bushfire season, which took place between June 2019 and May 2020, was a series of megafires that occurred along the southeast coastline of Australia. It was one of the largest fire complexes in Australian history, with more than 44.5 million acres affected. Most of the fires happened in New South Wales, including the Gospers mountain fire, which was the largest forest fire ever recorded in Australia. Satellite images show that these fires started in late October 2019 and ended in late January 2020. During this period, ASTER captured approximately 1000 frames of nighttime observations over the southeastern coastline of Australia, containing multiple fire observations that can be used to evaluate the performance of the FILDA-2 product.

Fig. S1 in the Supplementary Material displays the distribution of fire pixels detected by FILDA-2 from August 1, 2019, to February 29, 2020, for the southeastern coastline of Australia. Zoomed-in plots show individual fire events that were captured by ASTER. Figs. 5 and 6 and Figs. S2 and S3 in the Supplementary Material provide two case studies, which are part of Fig. S1 in the Supplementary Material, that demonstrate the superior performance of FILDA-2. Figs. 5 and 6 compare the fire detections of FILDA-2, AF-I, and FILDA-1, while Figs. S2 and S3 in the Supplementary Material compare the fire detections of FILDA-2, AF-I, and AF-M. The two case studies show that FILDA-2 has a slightly better performance than AF-I (Figs. 5 and 6), as more isolated fire pixels confirmed by ASTER were detected for a clearer delineation of the fire lines by FILDA-2. It is also evident that FILDA-2 outperforms both FILDA-1 (Figs. 5 and 6) and AF-M (Figs. S2 and S3 in the Supplementary Material) in fire detection, as only a limited number of fires were detected by FILDA-1 and AF-M in these two cases. The improvement of FILDA-2 can be attributed to the inclusion of nighttime visible light information through the temporal probability test, which enables the use of more relaxed thresholds in the contextual test of IR data. We will delve into this topic in greater depth in the subsequent paragraphs.

For example, Fig. 5 shows an isolated fire incident (highlighted by the orange circle) around 5 km away from the fire front on January 8, 2020. While the presence of this fire can be easily verified through both VJ1 Level-1B observation with a near-nadir view and the ATSTER observation at a resolution of around 90 m, AF-I failed to detect the fire since the cooler BT_{I4} of 293 K for this fire pixel at the VNP view angle of 65° does not meet the criteria for identifying it as a fire pixel candidate. At this view angle, the signal of fires is averaged across a larger pixel area compared to the nadir view of VJ1 or ASTER. The weaker fire signal would make this fire pixel also fail to pass the contextual test if a 3-σ criterion were applied. In contrast, FILDA-2 recognized this pixel as a visible light anomaly in the DNB imagery at a confidence level of 0.99 when compared with the nighttime visible light climatology, allowing it to be classified as a valid fire pixel candidate. Consequently, the thresholds for the subsequent tests were relaxed to a 2.5-σ level and the pixel was ultimately classified as a fire spot.

Another example shown in Fig. 6 occurred on January 3, 2020, when fires were present within a relatively warmer background scene. The $\overline{BT}_{I4b}$ in 5-km range was 295.5 K, with a MAD($\overline{BT}_{I4b}$) value of 0.95 K, and the corresponding $\overline{\Delta BT}_{I45b}$ and MAD($\overline{\Delta BT}_{I45b}$) were 2.96 K and 0.43 K, respectively.

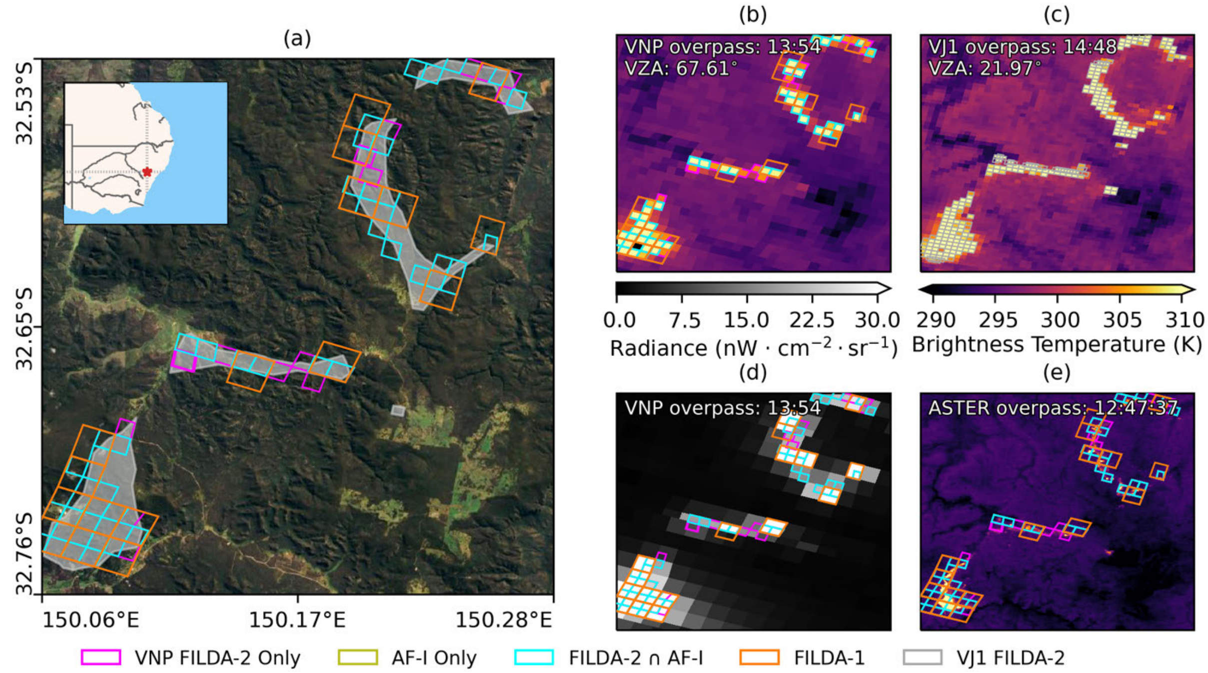

Fig. 6. Multiband and multisensor view of the black summer bushfire on January 3, 2020, by VIIRS and ASTER. (a) Google image of the fire event. (b) VNP I-band 3.74 μm BT at 13:54 UTC; the averaged view zenith angle is ~67.6°. (c) VJ1 I-band 3.74 μm BT at 14:48 UTC with a view zenith angle of 22°. (d) Same as (b) but for resampled DNB observation at M-band resolution. (e) ASTER 8.3 μm image overpass at 12:47 UTC. The boxes on the images indicate the fire pixel footprints color-coded according to their corresponding detection algorithms. FILDA-2 VJ1 detection in (c) is displayed as light-gray-shaded areas in (a). The resolution of FILDA-2 (VNP and VJ1) and AF-I detection are 375 m, and FILDA-1 resolution is 750 m. The orange circle indicates that FILDA-2 better delineated the fire front in the Northeast. The green circle indicates potential isolated fire spots omitted by both FILDA-2 and AF-I. See text for detail.

Although the absolute temperature of the pixels was high (>305 K), the relatively small difference of approximately 8.88 K between the ΔBT_{I45} of those fire pixels and the background $\overline{\Delta BT}_b$ prevented the AF-I algorithm from identifying them as fires. However, in FILDA-2, visible light information from DNB played a strong constraint in the selection of the fire pixel candidates, allowing the thresholds of BT difference to be relaxed down to 7.5 K and enabling the detection of the fire. This resulted in a more accurate depiction of the fire front, as shown in the orange circle in Fig. 6.

More examples supporting the conclusion earlier can be found in Fig. S1 in the Supplementary Material. While the information from the nighttime visible light measurements enhanced the ability of FILDA-2 to detect smaller and cooler fires, missed detection can still occur, as demonstrated by the isolated hot spot highlighted by the green circle of Fig. 6. Although the DNB information helped to identify the isolated spot as a potential fire candidate, the relatively low BT_{I4} of 298.6 K only resulted in a 1.06-σ level of significance through (10) in the contextual test. Despite achieving 3.15-σ and 6.39-σ levels of significance could be obtained through (9) and (11), respectively, the joint possibility of the isolated spot being a thermal anomaly was 0.85, which did not meet the required confidence level of 0.99. Consequently, FILDA-2 rejected it from being recognized as a fire. However, the VJ1 FILDA-2 product was able to detect this particular fire pixel, as shown as the pink shaded area in Fig. 6(a) as well as in Fig. 6(c) due to its near-nadir view for this event.

The current operation synergy between the VNP and VJ1 allows for the VIIRS to observe the Earth at a near-nadir view within a one-hour window, in contrast to the 3-h lag in the MODIS Terra and Aqua constellation. In addition to serving as a supplement to the VNP detection, the synergistic use of the VNP and VJ1 fire products also offers the opportunity to investigate the impact of view geometry on the contextual test of a fire detection algorithm, which may have contributed to the aforementioned missed detection. This will be a potential future improvement of FILDA-2.

B. Case Validation of the MCE

While it is ideal to measure CO and CO_2 to directly validate the MCE, it is prohibitively difficult to collect those measurements over a fire pixel at night, particularly when considering the need to have multiple days of ground measurements within the satellite overpass time, which is necessary to form a statistically significant assessment.

The most recent studies investigated the usage of MDR, derived from the daytime TROPOMI NO_2 to CO ratio, to estimate combustion efficiency [8], [88]. These data show that the MDR resonates with the combustion status (MCE): a higher MDR over a fire corresponds to a higher MCE associated with high-temperature flaming combustion, while a lower MDR indicates low-temperature smoldering combustion. Following this concept, we used the hourly CO and NO_2 data measured by the three EPA sites located in North Los Angles during 6~21 September 2022, when the Bobcat fires around the Angeles National Forest were within a 5-km radius of these measurement sites. The background diurnal climatology of CO

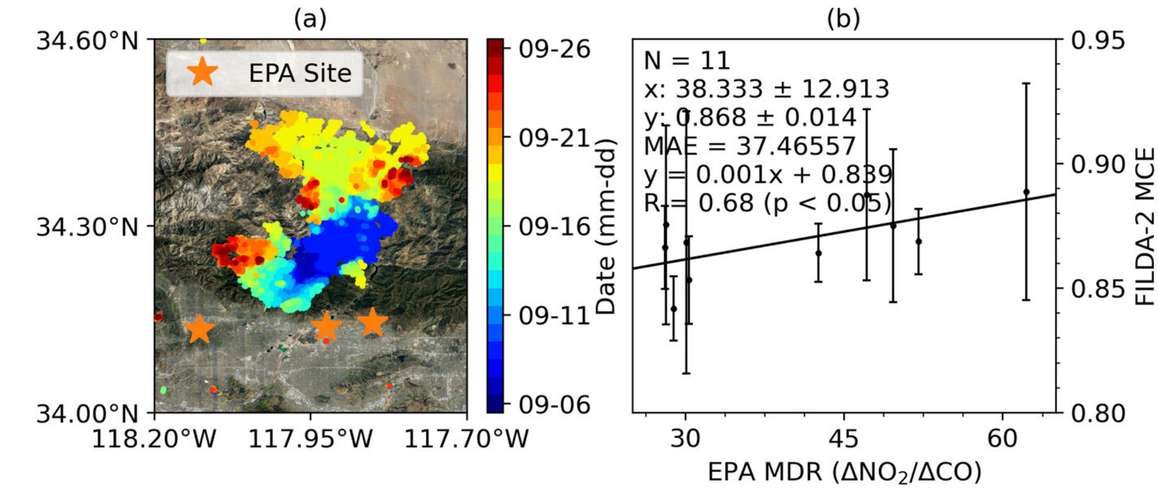

Fig. 7. Assessment of FILDA-2 MCE with EPA NO_2 and CO data for the Bobcat fire in Angeles National Forest, California, USA, 2020. (a) Fire progression map of the Bobcat fire. (b) Scatter plot of the MDR between NO_2 and CO as measured by EPA versus FILDA-2 MCE. See text for details.

and NO_2 was derived from July 2022 when no significant wildfires were occurring.

We derived the EPA-based MDR through

$$\mathrm{MDR} = \frac{\Delta NO_2}{\Delta CO} \tag{18}$$

where the ΔNO_2 is the concentration of the fire-emitted NO_2, it was obtained by subtracting the background NO_2 concentration from the real-time measurements of NO_2 concentration during the period of the fires events. ΔCO is the concentration of fire-emitted CO obtained through the same approach as NO_2. A 3-h moving average of MDR centered at the VIIRS overpass time was obtained and used as a proxy of in situ MCE for the evaluation of satellite-based MCE. Wind direction from the MERRA-2 dataset was used to select the days of observation for the comparison. Fig. 7(b) shows a scatter plot comparing the EPA-MDR and FILDA-2 MCE. The data demonstrate a positive correlation between the EPA-MDR and FILDA-2 MCE. While the correlation coefficient is modest $\sim$0.68, it is statistically significant ($p < 0.05$). Taking into consideration the resolution of the EPA CO measurement is only 0.01 ppb, the 5-km distance between the fire location and EPA sites, and the statistical bulk method applied to the MCE, it is reasonable to conclude that the FILDA-2 MCE change does resonate with the change of burning phases and can be used to represent the combustion efficiency. Future field campaigns will be necessary to explore this idea further.

C. Global Comparison Between FILDA-2 and AF-I Products

Globally, the FILDA-2 product outperforms AF-I in fire detection. Table III summarizes the detected fire of FILDA-2 and AF-I from August 2019 to October 2019 on a global scale in the three M-band aggregation zone. The scan angle boundaries are provided at the bottom of Table III. In general, after removing the bow-tie-affected fire pixels (discussed in the following), no significant omission of fires happened in FILDA-2 compared with AF-I. Indeed, FILDA-2 was able to pick out 25.37% more nighttime thermal anomalies when compared with AF-I. That fraction increased to 32.27% in areas viewed

TABLE III

COUNTS OF DETECTED HOTSPOT PIXELS FROM FILDA-2 AND AF-I AS A FUNCTION OF AGGREGATION ZONE

Algorithm	1:1 Zone	2:1 Zone	3:1 Zone	Total
Detected by both	261,379	115,162	129,984	506,525
FILDA-2 only	56,468	30,107	41,943	128,518
(Fraction)	(21.62%)	(26.11%)	(32.27%)	(25.37%)
AF-I only	1,357	626	672	2,455
(Fraction)	(0.52%)	(0.54%)	(0.36%)	(0.48%)
Scan angle edge	0° ⟵⟶ 31.72 °	⟵⟶ 44.86°	⟵⟶ 56.28°	

by the M-band aggregation zone 3, where pixel sizes are up to four times larger than the nadir. As aforementioned, a larger pixel size dilutes the fire signal and consequently reduces the chance of the fire pixel being detected. The rising fraction of fire pixels as compared with the AF-I indicates that the angular dependence of the fire detection was mitigated in FILDA-2 when DNB information is utilized in the detection process. This will be further examined and explained in Fig. 11. The distributions of BT_{I4} and ΔBT_{I45} for fire pixels detected by FILDA-2 and AF-I are shown in Fig. 8. Noticeable in Fig. 8(a) are the much smoother boundaries of BT_{I4} and ΔBT_{I45} for segregating the thermal anomalies (with $p < 0.005$) and the fire-free background. The smooth boundaries benefit from the fact that all the thresholds applied in FILDA-2 are dynamically determined, indicating that commonly used absolute thresholds for selecting the fire candidates in AF-I are too rigid. In contrast, the temperature distribution of the AF-I fire pixels presents sharp boundaries, as shown in Fig. 8(b), indicating that the possibility of recognizing smaller and cooler fires is eliminated due to the fixed thresholds that AF-I applies, as shown in Fig. 5.

As aforementioned, FILDA-2 detected a total of 128 518 (25.37%) more fire pixels than AF-I. Closer analysis reveals that those extra hot spots detected by FILDA-2 can be categorized into two types. The first type, known as type-I, consists of the isolated fire pixels for which there is no companion AF-I fire found, as shown in Fig. 5. The second

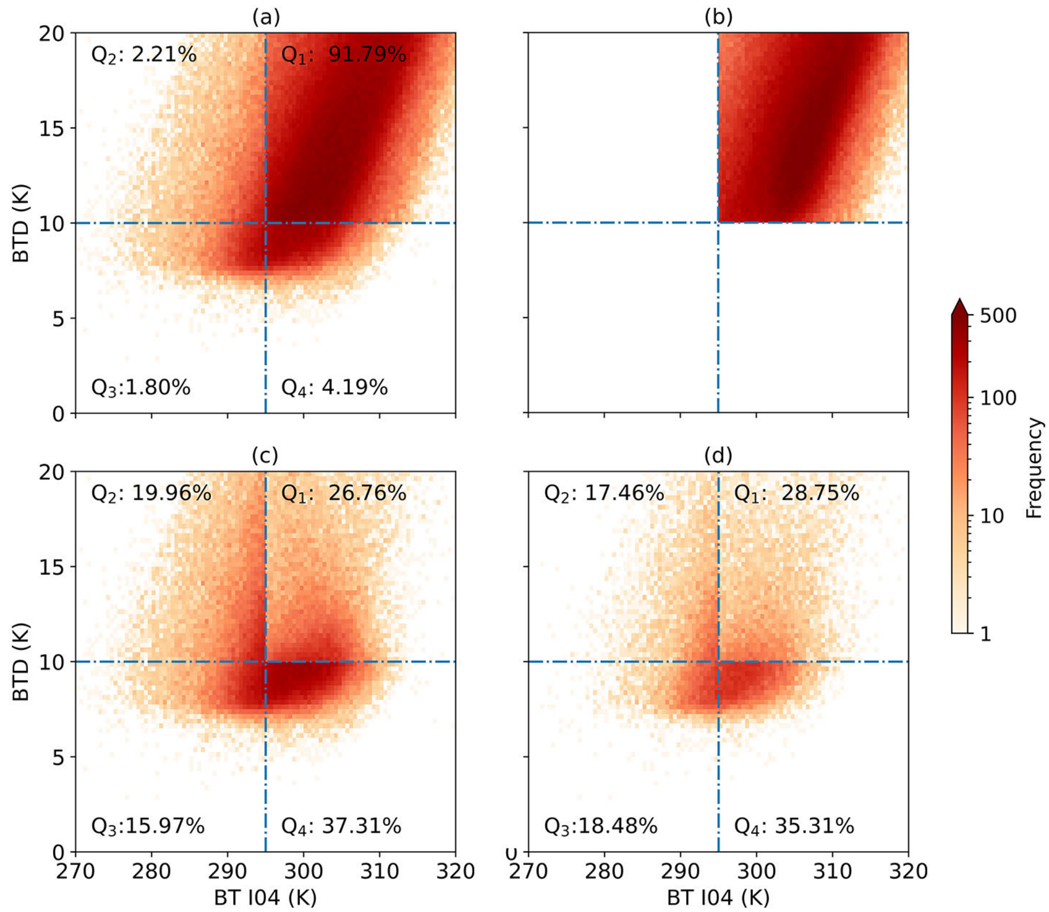

Fig. 8. Two-dimensional temperature distribution of the fire detected by different algorithms. The x-axis is the 3.74 μm BT (BT_{I4}). The y-axis is the BT difference between the 3.74 and 11.45 μm (ΔBT_{I45}). (a) For all the fire pixels detected by FILDA-2 algorithm. (b) For all the fire pixels detected by AF-I algorithm. (c) For fire pixels detected by FILDA-2 only (type-I and type-II). (d) For type-I fires detected by FILDA-2 only. See text for details.

type, known as type-II, is the fire pixel neighboring at least one AF-I fire pixel. While it is expected that relaxed thresholds would lead to the detection of more type-II fires, the detection of type-I fires is particularly noteworthy, as it demonstrates the superior performance of FILDA-2 (as shown in Fig. 5). The temperature distribution of those fires only detected by FILDA-2 (type-I + type-II) is shown in Fig. 8(c), among which 43.13% were type-II fires and 56.87% were isolated fires. The temperature distribution of the type-I fire (only detected by FILDA-2 with no AF-I neighbored) is shown in Fig. 8(d). While quadrant II to quadrant IV contains pixels that were not selected by AF-I as fire candidates but were selected and proved to be significantly warmer than the surrounding by FILDA-2, it is interesting to see that ∼28.75% (12 171) of pixels remain in the quadrant I, which was fire candidates that selected initially but subsequently failed to pass the contextual tests in AF-I algorithm. Carefully examining the AF-I algorithm QA for those pixels revealed that 97.8% (11 900) of the quadrant I pixels were initially included as the fire candidates. For the remaining 2.2%, no specific reason for their exclusion in the AF-I algorithm could be found. Based on our data examination, their BT_{I4} and ΔBT_{I45} all surpassed the absolute thresholds of 320 K and 10 K. Among the 11 900 candidates, 11.73% (1396) were persistent heat sources near/over the water surface that passed all three contextual tests but were

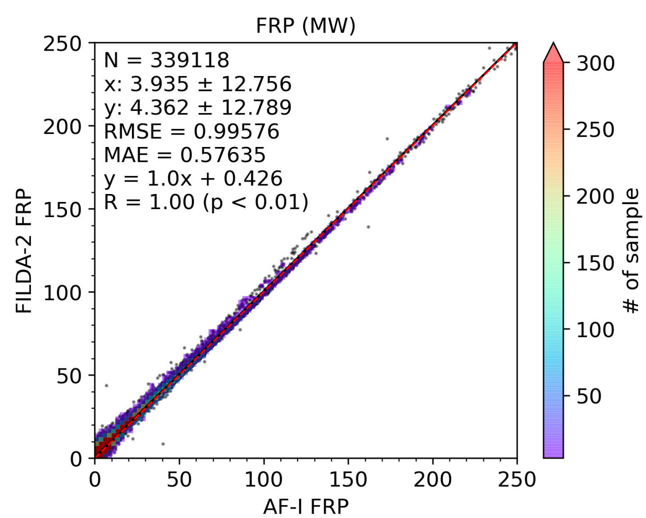

Fig. 9. FRP comparison between the VNP FILDA-2 and AF-I data product for August 2019–October 2019. See text for details.

simply excluded because of their near-water/over-water nature. A value of 82.84% failed to pass one or more contextual tests in AF-I but was picked up by FILDA-2 due to the relaxed MWIR thresholds enabled by the DNB information.

To evaluate the accuracy of the FRP calculation for FILDA-2, a point-by-point comparison of FRP values was

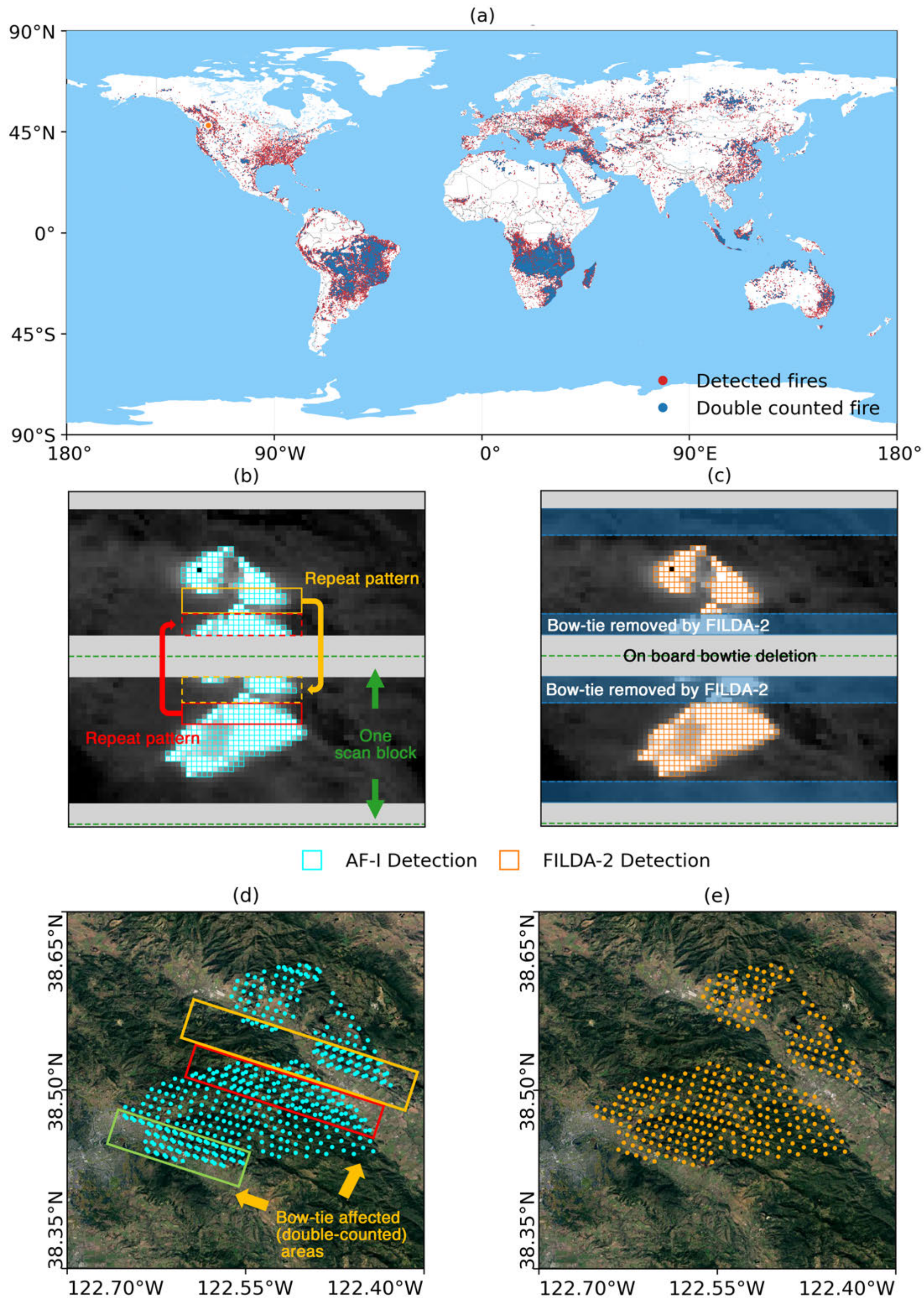

Fig. 10. Illustration of the bow-tie effect on the double counting of fire pixels. (a) Global view of the AF-I fire detection, note in FILDA-2 the bow-tie-affected fire pixels are well recognized and removed for August–October 2019). (b) Example in double counting of fire detection in AF-I, two repeated patterns are highlighted by the broken line boxes. (c) Same area as (b) but for FILDA-2 product. (d) Same as (b) but is projected on Earth's surface. (e) Same as (c) but is projected on Earth's surface. The orange and red boxes in (d) indicate the bow-tie-affected observations shown in (a). The green box shows bow-tie-affected areas for another consecutive VIIRS scan block that is not shown in (a). See text for details.

conducted for fires detected by both AF-I and FILDA-2, as shown in Fig. 9. As aforementioned, the FRP is derived based on the M-band 4.05 μm observation (742 m) considering the saturation nature of the I-band 3.74 μm. Then, M-band FRP is distributed equally into the I-band fire pixels. In order to make a fair comparison, the I-band FRP is summed back to the M-band resolution. As shown in Fig. 9, the FRP calculation of FILDA-2 and AF-I can be viewed as identical since they are

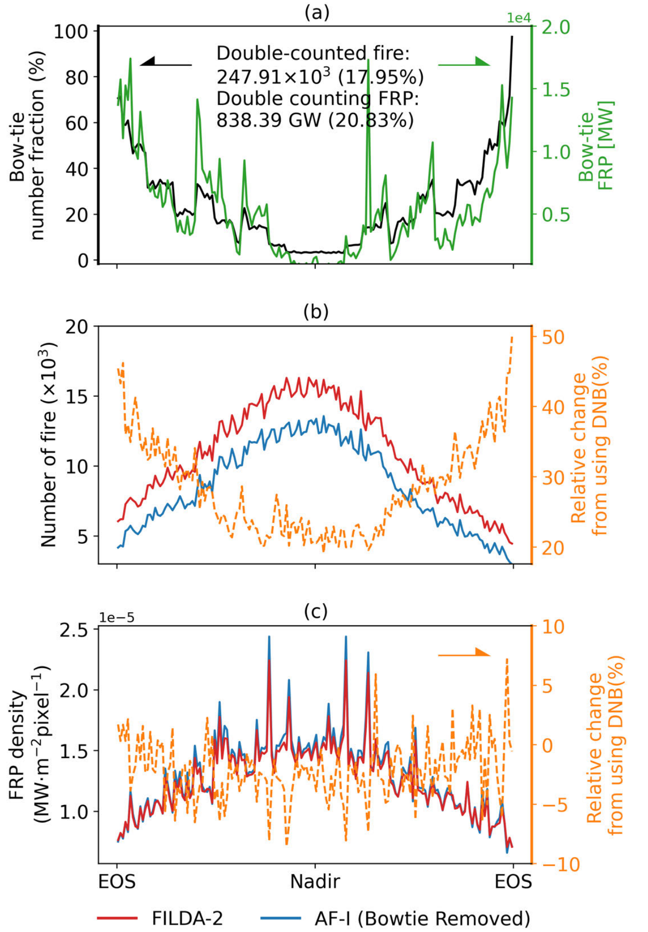

Fig. 11. Angular distribution (from nadir to the end of scan or EOS) of different fire products. (a) For FRP and number fraction of the AF-I bow-tie-affected fire pixels. (b) For the number of fires detected by the AF-I (after removing the bow-tie-affected fire pixels, blue line) and by FILDA-2 (red line). (c) Same as (b) but for the FRP density. See text for details.

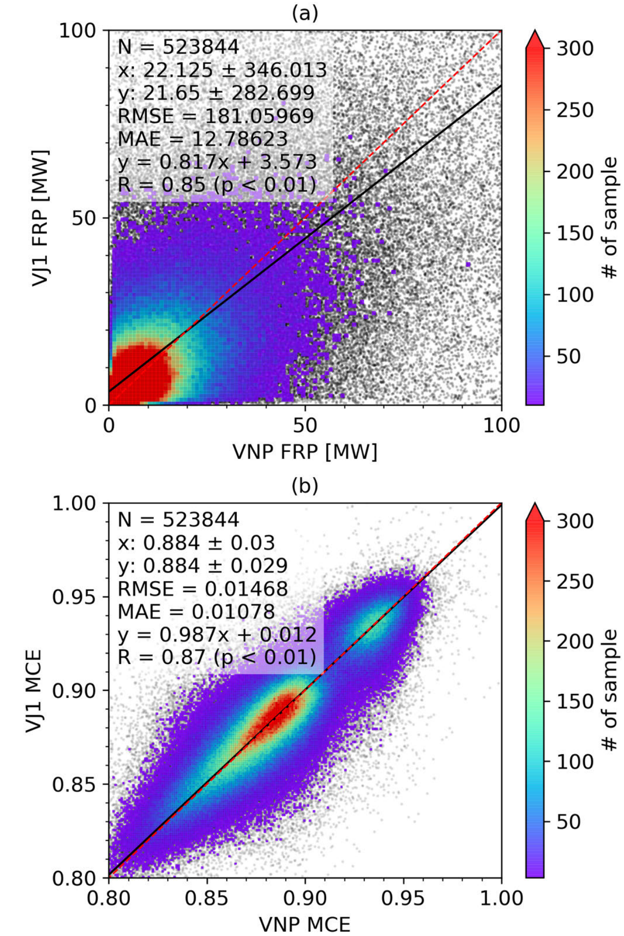

Fig. 12. Inter-comparison of FRP and MCE between VNP and VJ1 FILDA-2 products. (a) Global FRP comparison. (b) Global MCE comparison. Fire data were resampled into a 0.25° × 0.25° climate modeling grid (CMG) for point-by-point comparison. The dashed red line is the one-to-one line and the solid black line is the best regression line. Colors underneath the scatter points represent the density of the data.

derived from the same physical formula and observations but only with different implementations. The slight difference can be explained by the different window sizes used to acquire the nonfire clear-sky pixels for calculating the background radiance.

Another improvement of the FILDA-2 products is the identification and removal of the bow-tie effect and the inter-scan overlap. While by design bow-tie-affected pixels are removed in the onboard aggregation process (i.e., prior to data transmitted to the surface), a significant amount of the residual overlapping pixels remains in the VIIRS level-1B dataset. A consequence of the residual is the double-counting of the fire pixels in bow-tie areas. Fig. 10 is the global fire detection of the AF-I algorithm from August 2019 to October 2019. The double-counted fires are marked with blue color. Fig. 10(b) demonstrates a fire event that was observed by VNP in two consecutive scan blocks. Squares in cyan are the AF-I detection. Two repeated patterns circled by the dashed rectangles could be easily discerned by comparing them with their solid line counterparts. In this case, 42% of the fires are double counted. FILDA-2 uses the DNB aggregation scheme Opt.32 as the reference frame to calculate the bow-tie index of the I- and M-bands (overlap ratio of the I-band and M-band pixels with DNB in the same scan block). Since no significant bow-tie effect and interscan overlap occur in Opt.32, a bow-tie index of 1 indicates that the pixel is free from the impact of the bow-tie effect. In general, a value of 0.85 is sufficient to remove most affected pixels while still preserving full coverage of Earth observations. Fig. 10(c) shows the fire detection of the FILDA-2. Clearly, the double-counted pixels have been effectively recognized and removed.

Fig. 11 shows a zoomed-in analysis of the bow-tie-affected fire pixels from August 2019 to October 2019, globally. Fig. 11(a) shows that the doubled-counted fire pixels can account for up to ∼18% of the total fires detected. The total FRP of these double-counted fires can reach up to 838 GW (20.83%), which is significant when applied to construct the emission inventories for the chemistry transport model. We applied the same technique to remove the doubled-counted fire pixels in the AF-I fire dataset. Fig. 11(b) shows the comparison of the number of detection for FILDA-2 and AF-I detection after bow-tie removal. We find that the detection

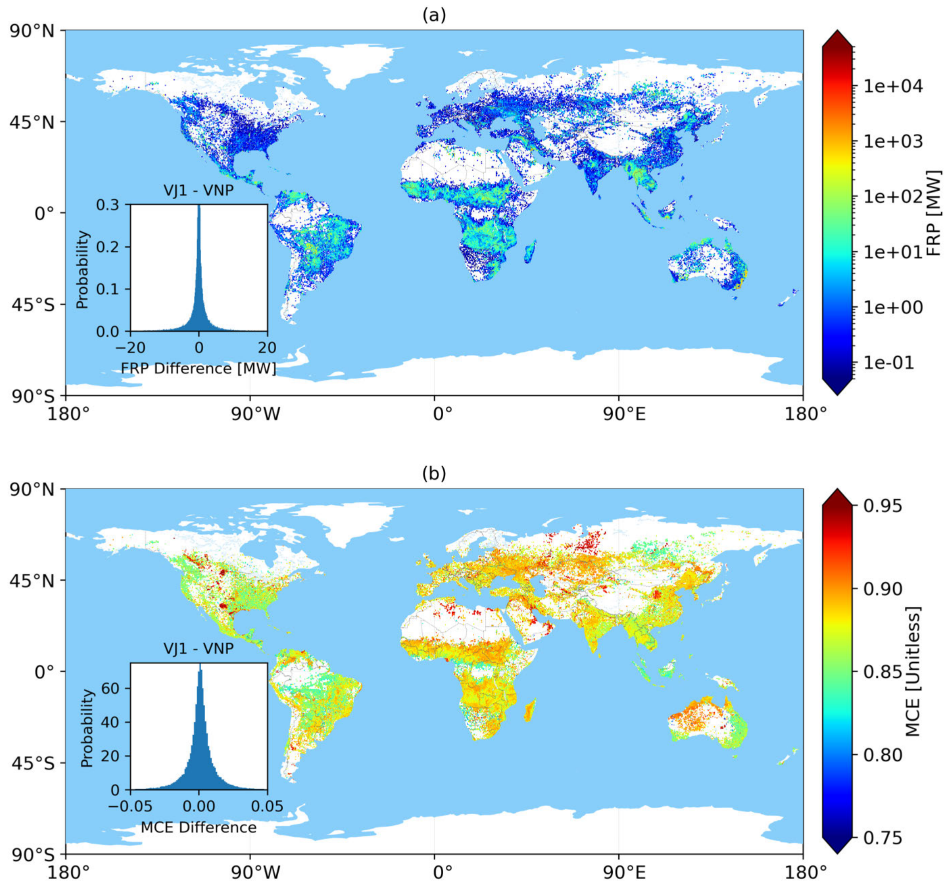

Fig. 13. Global distribution of FRP and MCE retrieved from VJ1 at night for August 2019–July 2020, averaged to a 0.25° × 0.25° CMG. (a) FILDA-2 VJ1 FRP distribution August 2019–July 2020. (b) FILDA-2 VJ1 MCE distribution August 2019–July 2020. The reddish grids on the MCE map over Siberia, the Middle East, North Dakota, and Texas are gas flaring of the petroleum industry indicating their flaming combustion status. Inset: Histogram of differences of (a) FRP and (b) MCE between VJ1 and VNP. Both of the histograms exhibit a Gaussian distribution with zero mean value indicating no systematic bias between VNP and VJ1 retrievals.

has a strong angular dependence and FILDA-2 was able to detect more fires toward the EOS, thus mitigating the angular dependence. Fig. 11(c) compares the averaged FRP density (i.e., FRP divided by the pixel area) of the FILDA-2 and AF-I products. Since FILDA-2 is able to detect cooler and smaller fires, it is reasonable to see that the majority of the FILDA-2 curve (red line) is below the AF-I curve (blue line). Moreover, since FILDA-2 detects more fire at the EOS, a subtle positive trend of relative increase is discernible when moving from the nadir to EOS, which indicates again that the angular dependence of the fire detection is mitigated.

D. VJI and VNP Results

The performance of VJ1 FILDA-2 was evaluated by comparing its FRP and MCE values to those of VNP. These parameters were investigated spatially at the 0.25° CMG to minimize the impact of the different footprints of the fires detected by VNP and VJ1. Fig. 12 shows the daily point-by-point comparison of VJ1 and VNP in terms of FRP and MCE. We see that the VJ1 FRP and MCE are highly correlated with their VNP counterparts (∼0.85 for FRP and ∼0.87 for MCE), with only a ∼2% mean bias difference in FRP and no bias in MCE. The slight discrepancy in the FRP can be explained by the following reasons. First, the difference of 50 minutes in overpass time may result in the two sensors sensing slightly different stages of the fire. Second, the difference in the view geometry of VJ1 and VNP can greatly impact the detection of fire, as shown in the previous discussion, and consequently, contribute to the differences in the FRP comparison. On the other hand, the MCE shows more robust statistics and concentrated distribution, since MCE is essentially derived from the VEF, which is less sensitive to the viewing geometry. Interestingly, there are two apparent clusters centering at 0.89 and 0.94 in the MCE scatter plot [Fig. 12(b)], indicating two unique combustion modes on the global scale, namely, the biomass burning and the gas flaring. It is also evident and reasonable to assume that the biomass-burning cluster should have a longer tail/radius compared with the gas-flaring cluster, considering that the combustion characteristics can vary greatly between different land surface types.

Taking the daily gridded data into the monthly average, Fig. 13 shows the monthly global distribution of the fire pixel density, FRP, and MCE of VJ1 detection. Their VNP counterparts are shown in Fig. S4 in the Supplementary Material. Fig. S5 in the Supplementary Material shows the FRP distribution of FILDA-2 and its counterpart Wang et al. [24]. It is evident that detections of FILDA-2 provide a larger fire spatial coverage (∼24.43%) compared with the value of ∼7.83% coverage of Wang et al. [24] on the global scale.

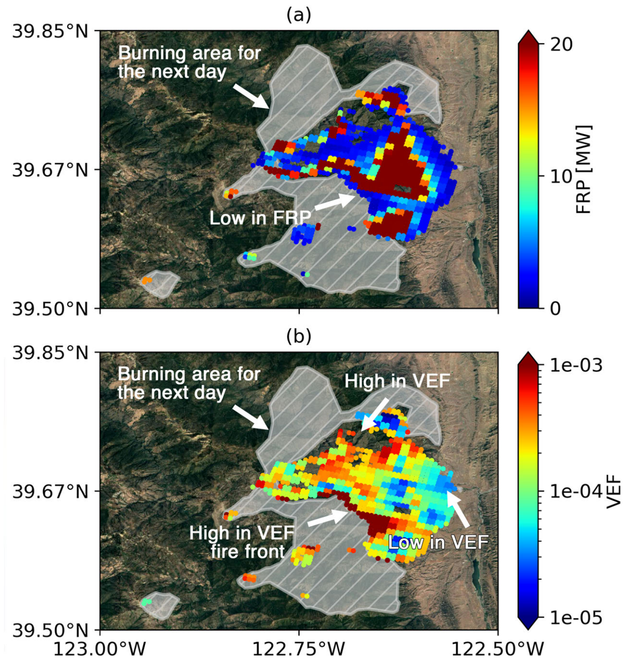

Fig. 14. Fire progression map of a fire event in California, on August 19, 2020. (a) FRP map of the fire event. (b) VEF map of the fire event. The shaded areas are the fire area detected by VIIRS on the following day (August 20, 2020).

The relative increase of the fire spatial coverage detected by FILDA-2 is ∼212%. North America, China, India, and Europe contribute the most to this increase, as more prescribed fires are detected in these regions. Furthermore, with the improvement made in FILDA-2, more gas flaring and mining-related burning activities are detected in areas, such as North Africa, North Dakota, and Texas in the U.S., the Persian Gulf of the Mideast, Siberia of Russia, and the northwest of China. Their conspicuously high MCEs make those areas in stark contrast to other biomass-burning activities, as shown in Fig. 13(b), providing the opportunity for quantifying the emission of fossil fuel (e.g., methane) burning from space. Moreover, the insets in Fig. 13 show the distribution of the monthly difference of FRP and MCE between VNP and VJ1 retrievals. For either FRP or MCE, the difference obeys a Gaussian shape distribution with a mean value around zero, indicating no significant systematic bias exists between VJ1 and VNP results.

E. Potential of the VEF for Monitoring Fire Line Progression

While FRP and MCE can be used to constrain the estimates of the chemical speciation of fire emissions, VEF also has the potential strength of indicating the progression of the fire line. Fig. 14 shows an example of a fire event that happened in California, in 2020. Fig. 14(a) is the FRP map on August 19, 2020, on which gray-shaded areas are the regions where the fire progressed on the following day (August 20, 2020). Since FRP only provides information on the total energy emitted by the fires in a pixel, no clear fire front can be defined based on the FRP map provided. Those pixels neighboring the perimeter of the fire pixels detected the following day had very low FRP values.

Because VEF is essentially an index of the energy distribution of the combustion, a clear fire front can be defined, as shown in Fig. 14(b). The VEF data show that the fire line progressed much faster to the southwest and northwest, where VEF was significantly higher than in other directions, such as to the east. This pattern of fire line is blurry on the FRP map. In fact, large FRP values may often occur at places that are distant from the active firefront. This is understood because as fire lines pass through an area, what is left behind the fire lines are smoldering fires. These smoldering fires have lower temperatures than active flaming fires, but they can have large spatial areas (as a result of the time persistence of smoldering combustion), which can, in turn, lead to larger FRP at the fire pixel level.

V. Conclusion

Following Polivka et al. [14] and Wang et al. [24], we have developed an FILDA-2 for nighttime fire identification and combustion efficiency characterization applicable to Suomi-NPP, NOAA-20, and future VIIRS instruments, which carry the DNB's low-light visible measurement. We have designed a generalized resampling scheme to effectively map the DNB level-1 data from VIIRS aboard VJ1, as well as any future satellites of the JPSS constellation, to the footprint of VIIRS M-band pixels. A historical nighttime light database was integrated into FILDA-2 to identify the visible light anomalies produced by fires. VIIRS observations from its I-band, TIR, and MWIR bands are included in the fire detection process for better detection accuracy.

ASTER nighttime imagery, VIIRS operational active fire detection products, and the EPA trace gas measurements were used to validate the fire detection and MCE obtained by FILDA-2. Case studies and the global assessments through VNP products indicate a significant improvement in detecting smaller and cooler fires of FILDA-2 compared with the AF-I and AF-M due to the usage of VIIRS DNB and I-band observations. While maintaining good consistency in the FRP calculation when compared with AF-I FRP, FILDA-2 also shows superior performance in minimizing the double counting of fire pixels caused by the interscan overlap (bow-tie) nature of the VIIRS observations. The potential application of MCE for fire emission estimates of NO_2 and CO was evaluated against the EPA's real-time in situ measurements for the first time. Global assessments of FILDA-2 show good consistency for VNP and VJ1 FRP and MCE.

While most of the thresholds applied in selecting fire candidates were dynamically determined in FILDA-2, those used in the contextual tests remain fixed and will be further investigated in future studies. Another potential future improvement would be to develop a set of view geometry-dependent thresholds for contextual tests by exploiting the near-nadir view fire detection within the one-hour window provided by the current VNP and VJ1 operation scheme.

The availability of the VEF, FRP, and MCE of FILDA-2 at the fire pixel level in near-real time provides new opportunities for using the satellite fire information to support tactical planning of wildfire control and the estimation of the chemical speciation of fire emission for air quality forecast and climate studies. Future development of FILDA-2 includes the study of the view geometry-dependent thresholds for contextual tests, the development of a method for daytime MCE estimation, and the impact of aerosol on MCE estimation.

ACKNOWLEDGMENT

The authors acknowledge the public availability of the visible infrared imaging radiometer suite and MODerate resolution Imaging Spectroradiometer data from the Earth Observing System Data and Information System (EOSDIS), National Aeronautics and Space Administration (NASA). They also acknowledge the United States Geological Survey (USGS), Washington, DC, USA, for the public availability of Advanced Spaceborne Thermal Emission and Reflection data. They also thank the Air Pollution Surveillance (NAPS) Program of the U.S. Environmental Protection Agency (EPA), Washington, for establishing and maintaining the EPA sites used in this investigation.

REFERENCES

[1] J. Dozier, "A method for satellite identification of surface temperature fields of subpixel resolution," *Remote Sens. Environ.*, vol. 11, pp. 221–229, Jan. 1981.

[2] Y. J. Kaufman, R. G. Kleidman, and M. D. King, "SCAR-B fires in the tropics: Properties and remote sensing from EOS-MODIS," *J. Geophys. Res., Atmos.*, vol. 103, no. D24, pp. 31955–31968, Dec. 1998.

[3] Y. J. Kaufman et al., "Potential global fire monitoring from EOS-MODIS," *J. Geophys. Res.*, vol. 103, pp. 32215–32238, Dec. 1998.

[4] C. Justice et al., "The MODIS fire products," *Remote Sens. Environ.*, vol. 83, nos. 1–2, pp. 244–262, 2002.

[5] I. Csiszar et al., "Active fires from the Suomi NPP Visible Infrared Imaging Radiometer Suite: Product status and first evaluation results," *J. Geophys. Res.*, vol. 119, pp. 803–816, Jan. 2014.

[6] W. Schroeder, P. Oliva, L. Giglio, and I. A. Csiszar, "The new VIIRS 375 m active fire detection data product: Algorithm description and initial assessment," *Remote Sens. Environ.*, vol. 143, pp. 85–96, Mar. 2014. [Online]. Available: http://www.sciencedirect.com/science/article/pii/S0034425713004483

[7] A. Darmenov and A. Da Silva, "The quick fire emissions dataset (QFED): Documentation of versions 2.1, 2.2 and 2.4," NASA Tech. Rep. Ser. Global Model. Data Assimilation, Goddard Space Flight Center, Greenbelt, MD, USA, Tech. Rep. NASA TM-AQ:5 2013-104606, 2013, p. 183, vol. 32.

[8] I. R. Van Der Velde et al., "Biomass burning combustion efficiency observed from space using measurements of CO and NO_2 by the tropospheric monitoring instrument (TROPOMI)," *Atmos. Chem. Phys.*, vol. 21, no. 2, pp. 597–616, 2021. [Online]. Available: https://acp.copernicus.org/articles/21/597/2021/

[9] C. Wiedinmyer et al., "The fire INventory from NCAR (FINN): A high resolution global model to estimate the emissions from open burning," *Geosci. Model Develop.*, vol. 4, no. 3, pp. 625–641, Jul. 2011. [Online]. Available: https://gmd.copernicus.org/articles/4/625/2011/

[10] C. Ichoku, L. Giglio, M. J. Wooster, and L. A. Remer, "Global characterization of biomass-burning patterns using satellite measurements of fire radiative energy," *Remote Sens. Environ.*, vol. 112, no. 6, pp. 2950–2962, Jun. 2008.

[11] M. J. Wooster et al., "LSA SAF Meteosat FRP products—Part 1: Algorithms, product contents, and analysis," *Atmos. Chem. Phys.*, vol. 15, no. 22, pp. 13217–13239, Nov. 2015. [Online]. Available: https://acp.copernicus.org/articles/15/13217/2015/

[12] M. J. Wooster, G. Roberts, G. L. W. Perry, and Y. J. Kaufman, "Retrieval of biomass combustion rates and totals from fire radiative power observations: FRP derivation and calibration relationships between biomass consumption and fire radiative energy release," *J. Geophys. Res.*, vol. 110, no. D24, pp. 1–24, 2005.

[13] G. A. Ferrada, M. Zhou, J. Wang, A. Lyapustin, Y. Wang, S. R. Freitas, and G. R. Carmichael, "Introducing the VIIRS-based fire emission inventory version 0 (VFEIv0)," *Geosci. Model Develop.*, vol. 15, no. 21, pp. 8085–8109, 2022.

[14] T. N. Polivka, J. Wang, L. T. Ellison, E. J. Hyer, and C. M. Ichoku, "Improving nocturnal fire detection with the VIIRS day–night band," *IEEE Trans. Geosci. Remote Sens.*, vol. 54, no. 9, pp. 5503–5519, Sep. 2016.

[15] T. A. Croft, "Burning waste gas in oil fields," *Nature*, vol. 245, pp. 375–376, Oct. 1973.

[16] L. Giglio, W. Schroeder, and C. O. Justice, "The collection 6 MODIS active fire detection algorithm and fire products," *Remote Sens. Environ.*, vol. 178, pp. 31–41, Jun. 2016.

[17] F. Li, X. Zhang, S. Kondragunta, C. C. Schmidt, and C. D. Holmes, "A preliminary evaluation of GOES-16 active fire product using Landsat-8 and VIIRS active fire data, and ground-based prescribed fire records," *Remote Sens. Environ.*, vol. 237, Feb. 2020, Art. no. 111600.

[18] D. Peterson, J. Wang, C. Ichoku, E. Hyer, and V. Ambrosia, "A sub-pixel-based calculation of fire radiative power from MODIS observations: 1 : Algorithm development and initial assessment," *Remote Sens. Environ.*, vol. 129, pp. 262–279, Feb. 2013.

[19] D. Peterson and J. Wang, "A sub-pixel-based calculation of fire radiative power from MODIS observations: 2. Sensitivity analysis and potential fire weather application," *Remote Sens. Environ.*, vol. 129, pp. 231–249, Feb. 2013.

[20] C. D. Elvidge, M. Zhizhin, F.-C. Hsu, and K. E. Baugh, "VIIRS nightfire: Satellite pyrometry at night," *Remote Sens.*, vol. 5, no. 9, pp. 4423–4449, 2013.

[21] D. Ward and L. Radke, "Emissions measurements from vegetation fires: A comparative evaluation of methods and results," in *Fire in the Environment: The Ecological, Atmospheric, and Climatic Importance of Vegetation Fires. Dahlem Workshop Reports: Environmental Sciences Research Report*, P. J. Crutzen and J. G. Goldammer, Eds. Chischester, U.K.: Wiley, 1993, pp. 53–76.

[22] D. E. Ward et al., "Effect of fuel composition on combustion efficiency and emission factors for African savanna ecosystems," *J. Geophys. Res., Atmos.*, vol. 101, no. D19, pp. 23569–23576, Oct. 1996.

[23] R. J. Ferek, J. S. Reid, P. V. Hobbs, D. R. Blake, and C. Liousse, "Emission factors of hydrocarbons, halocarbons, trace gases and particles from biomass burning in Brazil," *J. Geophys. Res., Atmos.*, vol. 103, no. D24, pp. 32107–32118, Dec. 1998.

[24] J. Wang et al., "Detecting nighttime fire combustion phase by hybrid application of visible and infrared radiation from Suomi NPP VIIRS," *Remote Sens. Environ.*, vol. 237, Feb. 2020, Art. no. 111466. [Online]. Available: http://www.sciencedirect.com/science/article/pii/S0034425719304857

[25] M. O. Andreae, "Emission of trace gases and aerosols from biomass burning—An updated assessment," *Atmos. Chem. Phys.*, vol. 19, no. 13, pp. 8523–8546, Jul. 2019. [Online]. Available: https://acp.copernicus.org/articles/19/8523/2019/

[26] R. J. Yokelson et al., "Coupling field and laboratory measurements to estimate the emission factors of identified and unidentified trace gases for prescribed fires," *Atmos. Chem. Phys.*, vol. 13, no. 1, pp. 89–116, Jan. 2013.

[27] S. P. Urbanski, "Combustion efficiency and emission factors for wildfire-season fires in mixed conifer forests of the northern Rocky Mountains, U.S.," *Atmos. Chem. Phys.*, vol. 13, no. 14, pp. 7241–7262, Jul. 2013.

[28] S. Collier et al., "Regional influence of aerosol emissions from wildfires driven by combustion efficiency: Insights from the BBOP campaign," *Environ. Sci. Technol.*, vol. 50, no. 16, pp. 8613–8622, Aug. 2016.

[29] X. Liu et al., "Airborne measurements of western U.S. wildfire emissions: Comparison with prescribed burning and air quality implications," *J. Geophys. Res., Atmos.*, vol. 122, no. 11, pp. 6108–6129, Jun. 2017. [Online]. Available: https://agupubs.onlinelibrary.wiley.com/doi/abs/10.1002/2016JD026315

[30] E.-A. Guérette et al., "Emissions of trace gases from Australian temperate forest fires: Emission factors and dependence on modified combustion efficiency," *Atmos. Chem. Phys.*, vol. 18, no. 5, pp. 3717–3735, Mar. 2018.

[31] V. Tihay-Felicelli, P. A. Santoni, G. Gerandi, and T. Barboni, "Smoke emissions due to burning of green waste in the Mediterranean area: Influence of fuel moisture content and fuel mass," *Atmos. Environ.*, vol. 159, pp. 92–106, Jun. 2017.

[32] S. Liu et al., "Aerosol single scattering albedo dependence on biomass combustion efficiency: Laboratory and field studies," *Geophys. Res. Lett.*, vol. 41, no. 2, pp. 742–748, Jan. 2014.

[33] R. P. Pokhrel et al., "Parameterization of single-scattering albedo (SSA) and absorption Ångströom exponent (AAE) with EC/OC for aerosol emissions from biomass burning," *Atmos. Chem. Phys.*, vol. 16, no. 15, pp. 9549–9561, 2016. [Online]. Available: https://acp.copernicus.org/articles/16/9549/2016/

[34] F. Zhang et al., "Sensitivity of mesoscale modeling of smoke direct radiative effect to the emission inventory: A case study in northern sub-saharan African region," *Environ. Res. Lett.*, vol. 9, no. 7, Jul. 2014, Art. no. 075002.

[35] X. Pan et al., "Six global biomass burning emission datasets: Intercomparison and application in one global aerosol model," *Atmos. Chem. Phys.*, vol. 20, no. 2, pp. 969–994, Jan. 2020.

[36] Y. Yamaguchi, A. B. Kahle, H. Tsu, T. Kawakami, and M. Pniel, "Overview of advanced spaceborne thermal emission and reflection radiometer (ASTER)," *IEEE Trans. Geosci. Remote Sens.*, vol. 36, no. 4, pp. 1062–1071, Jul. 1998.

[37] C. Schueler, J. Clement, P. Ardanuy, C. Welsch, F. DeLuccia, and H. Swenson, "NPOESS VIIRS sensor design overview," *Proc. SPIE*, vol. 4483, pp. 11–23, Jan. 2012.

[38] R. E. Wolfe, G. Lin, M. Nishihama, K. P. Tewari, J. C. Tilton, and A. R. Isaacman, "Suomi NPP VIIRS prelaunch and on-orbit geometric calibration and characterization," *J. Geophys. Res., Atmos.*, vol. 118, no. 20, pp. 508–511, Oct. 2013.

[39] X. Xiong et al., "VIIRS on-orbit calibration methodology and performance," *J. Geophys. Res., Atmos.*, vol. 119, no. 9, pp. 5065–5078, 2014.

[40] X. Xiong et al., "Performance assessments and comparisons of S-NPP and NOAA-20 (JPSS-1) VIIRS on-orbit calibration," in *Proc. SPIE*, vol. 10785, 2018, pp. 192–204.

[41] T. N. Polivka, E. J. Hyer, J. Wang, and D. A. Peterson, "First global analysis of saturation artifacts in the VIIRS infrared channels and the effects of sample aggregation," *IEEE Geosci. Remote Sens. Lett.*, vol. 12, no. 6, pp. 1262–1266, Jun. 2015.

[42] S. D. Miller et al., "Illuminating the capabilities of the suomi national polar-orbiting partnership (NPP) Visible Infrared Imaging Radiometer Suite (VIIRS) day/night band," *Remote Sens.*, vol. 5, no. 12, pp. 6717–6766, Nov. 2013.

[43] L. Liao, S. Weiss, S. Mills, and B. Hauss, "Suomi NPP VIIRS day-night band on-orbit performance," *J. Geophys. Res., Atmos.*, vol. 118, no. 22, pp. 705–712, 2013.

[44] A. P. Cracknell, *Advanced Very High Resolution Radiometer AVHRR*. Boca Raton, FL, USA: CRC Press, 1997.

[45] W. L. Barnes and V. V. Salomonson, "MODIS: A global imaging spectroradiometer for the earth observing system," in *Proc. SPIE*, vol. 10269, 1992, pp. 280–302.

[46] R. E. Wolfe, D. P. Roy, and E. Vermote, "MODIS land data storage, gridding, and compositing methodology: Level 2 grid," *IEEE Trans. Geosci. Remote Sens.*, vol. 36, no. 4, pp. 1324–1338, Jul. 1998.

[47] A. M. Sayer, N. C. Hsu, and C. Bettenhausen, "Implications of MODIS bow-tie distortion on aerosol optical depth retrievals, and techniques for mitigation," *Atmos. Meas. Techn.*, vol. 8, no. 12, pp. 5277–5288, Dec. 2015.

[48] C. Cao, M. Weinreb, and H. Xu, "Predicting simultaneous nadir overpasses among polar-orbiting meteorological satellites for the intersatellite calibration of radiometers," *J. Atmos. Ocean. Technol.*, vol. 21, no. 4, pp. 537–542, 2004.

[49] E. C. Stokes et al., "Retired satellites: A chance to shed light," *Science*, vol. 373, no. 6562, pp. 1451–1452, Sep. 2021, doi: 10.1126/science.abl9965.

[50] B. Ramachandran, K. Chiang, and G. Lin. *VNP02DNB—VIIRS/NPP Day/Night Band Moderate Resolution 6-Min L1B Swath 750 m*. National Aeronautics and Space Administration Goddard Space Flight Center. Greenbelt, Maryland, United States. Accessed: Apr. 6, 2023. [Online]. Available: https://ladsweb.modaps.eosdis.nasa.gov/missions-and-measurements/products/VNP02DNB

[51] B. Ramachandran, K. Chiang, and G. Lin. *VJ102DNB—VIIRS/JPSS1 Day/Night Band Moderate Resolution 6-Min L1B Swath 750 m*. National Aeronautics and Space Administration Goddard Space Flight Center. Greenbelt, Maryland, United States. Accessed: Apr. 6, 2023. [Online]. Available: https://ladsweb.modaps.eosdis.nasa.gov/missions-and-measurements/products/VJ102DNB

[52] B. Ramachandran, K. Chiang, and G. Lin. *VNP03DNB—VIIRS/NPP Day/Night Band Moderate Resolution Terrain-Corrected Geolocation 6-Min L1 Swath 750 m*. National Aeronautics and Space Administration Goddard Space Flight Center. Greenbelt, Maryland, United States. Accessed: Apr. 6, 2023. [Online]. Available: https://ladsweb.modaps.eosdis.nasa.gov/missions-and-measurements/products/VNP03DNB

[53] B. Ramachandran, K. Chiang, and G. Lin. *VJ103DNB—VIIRS/JPSS1 Day/Night Band Moderate Resolution Terrain-Corrected Geolocation 6-Min L1 Swath 750 m*. National Aeronautics and Space Administration Goddard Space Flight Center. Greenbelt, Maryland, United States. Accessed: Apr. 6, 2023. [Online]. Available: https://ladsweb.modaps.eosdis.nasa.gov/missions-and-measurements/products/VJ103DNB

[54] B. Ramachandran, K. Chiang, and G. Lin. *VNP02MOD—VIIRS/NPP Moderate Resolution 6-Min L1B Swath 750 m*," National Aeronautics and Space Administration Goddard Space Flight Center. Greenbelt, Maryland, United States. Accessed: Apr. 6, 2023. [Online]. Available: https://ladsweb.modaps.eosdis.nasa.gov/missions-and-measurements/products/VNP02MOD

[55] B. Ramachandran, K. Chiang, and G. Lin. *VJ102MOD—VIIRS/JPSS1 Moderate Resolution 6-Min L1B Swath 750 m*. National Aeronautics and Space Administration Goddard Space Flight Center. Greenbelt, Maryland, United States. Accessed: Apr. 6, 2023. [Online]. Available: https://ladsweb.modaps.eosdis.nasa.gov/missions-and-measurements/products/VJ102MOD

[56] B. Ramachandran, K. Chiang, and G. Lin. *VNP03MOD—VIIRS/NPP Moderate Resolution Terrain-Corrected Geolocation 6-Min L1 Swath 750 m*. National Aeronautics and Space Administration Goddard Space Flight Center. Greenbelt, Maryland, United States. Accessed: Apr. 6, 2023. [Online]. Available: https://ladsweb.modaps.eosdis.nasa.gov/missions-and-measurements/products/VNP03MOD

[57] B. Ramachandran, K. Chiang, and G. Lin. *VNP02IMG—VIIRS/NPP Imagery Resolution 6-Min L1B Swath 375 m*. National Aeronautics and Space Administration Goddard Space Flight Center. Greenbelt, Maryland, United States. Accessed: Apr. 6, 2023. [Online]. Available: https://ladsweb.modaps.eosdis.nasa.gov/missions-and-measurements/products/VNP02IMG

[58] B. Ramachandran, K. Chiang, and G. Lin. *VJ102IMG—VIIRS/JPSS1 Imagery Resolution 6-Min L1B Swath 375 m*. National Aeronautics and Space Administration Goddard Space Flight Center. Greenbelt, Maryland, United States. Accessed: Apr. 6, 2023. [Online]. Available: https://ladsweb.modaps.eosdis.nasa.gov/missions-and-measurements/products/VJ102IMG

[59] B. Ramachandran, K. Chiang, and G. Lin. *VNP03IMG—VIIRS/NPP Imagery Resolution Terrain-Corrected Geolocation 6-Min L1 Swath 375 m*. National Aeronautics and Space Administration Goddard Space Flight Center. Greenbelt, Maryland, United States. Accessed: Apr. 6, 2023. [Online]. Available: https://ladsweb.modaps.eosdis.nasa.gov/missions-and-measurements/products/VNP03IMG

[60] B. Ramachandran, K. Chiang, and G. Lin. *VJ103IMG—VIIRS/JPSS1 Imagery Resolution Terrain-Corrected Geolocation 6-Min L1 Swath 375 m*. National Aeronautics and Space Administration Goddard Space Flight Center. Greenbelt, Maryland, United States. Accessed: Apr. 6, 2023. [Online]. Available: https://ladsweb.modaps.eosdis.nasa.gov/missions-and-measurements/products/VJ103IMG

[61] H. Oudrari et al., "Prelaunch Radiometric characterization and calibration of the S-NPP VIIRS sensor," *IEEE Trans. Geosci. Remote Sens.*, vol. 53, no. 4, pp. 2195–2210, Apr. 2015.

[62] J. Gledhill, "Aeronomic effects of the south Atlantic anomaly," *Rev. Geophys.*, vol. 14, no. 2, pp. 173–187, 1976.

[63] S. Casadio and O. Arino, "Monitoring the south Atlantic anomaly using ATSR instrument series," *Adv. Space Res.*, vol. 48, no. 6, pp. 1056–1066, Sep. 2011. [Online]. Available: https://www.sciencedirect.com/science/article/pii/S0273117711003267

[64] C. Elvidge, M. Zhizhin, K. Baugh, and F.-C. Hsu, "Automatic boat identification system for VIIRS low light imaging data," *Remote Sens.*, vol. 7, no. 3, pp. 3020–3036, Mar. 2015. [Online]. Available: https://www.mdpi.com/2072-4292/7/3/3020

[65] N. Baker and H. Kilcoyne, "Joint polar satellite system (JPSS) VIIRS radiometric calibration algorithm theoretical basis document (ATBD)," Goddard Space Flight Center, Greenbelt, MA, USA, Tech. Rep. 474-00027, 2013.

[66] M. O. Román et al., "NASA's black marble nighttime lights product suite," *Remote Sens. Environ.*, vol. 210, pp. 113–143, Jun. 2018. [Online]. Available: https://www.sciencedirect.com/science/article/pii/S003442571830110X

[67] Z. Wang, M. O. Román, V. L. Kalb, S. D. Miller, J. Zhang, and R. M. Shrestha, "Quantifying uncertainties in nighttime light retrievals from suomi-NPP and NOAA-20 VIIRS day/night band data," *Remote Sens. Environ.*, vol. 263, Sep. 2021, Art. no. 112557. [Online]. Available: https://www.sciencedirect.com/science/article/pii/S0034425721002777

[68] R. Lucchesi, "File specification for geos-5 FP (forward processing)," Nat. Aeronaut. Space Admin., Goddard Space Flight Center, Greenbelt, MD, USA, Tech. Rep. GSFC-E-DAA-TN19791, 2013.

[69] K. Didan. *MOD13C2 MODIS/Terra Vegetation Indices Monthly L3 Global 0.05 Deg CMG V006*. National Aeronautics and Space Administration Goddard Space Flight Center. Greenbelt, Maryland, United States. Accessed: Apr. 6, 2023. [Online]. Available: https://lpdaac.usgs.gov/products/mod13c2v006/

[70] A. R. Huete, K. Didan, T. Miura, E. P. Rodriguez, X. Gao, and L. G. Ferreira, "Overview of the radiometric and biophysical performance of the MODIS vegetation indices," *Remote Sens. Environ.*, vol. 83, nos. 1–2, pp. 195–213, 2002. [Online]. Available: https://www.sciencedirect.com/science/article/pii/S0034425702000962

[71] S. P. Abercrombie and M. A. Friedl, "Improving the consistency of multitemporal land cover maps using a hidden Markov model," *IEEE Trans. Geosci. Remote Sens.*, vol. 54, no. 2, pp. 703–713, 2016.

[72] M. A. Friedl et al., "Global land cover mapping from MODIS: Algorithms and early results," *Remote Sens. Environ.*, vol. 83, nos. 1–2, pp. 287–302, 2002.

[73] J. Xu, P. J. Morris, J. Liu, and J. Holden, "PEATMAP: Refining estimates of global peatland distribution based on a meta-analysis," *CATENA*, vol. 160, pp. 134–140, Jan. 2018. [Online]. Available: https://www.sciencedirect.com/science/article/pii/S0341816217303004

[74] Y. Hu, N. Fernandez-Anez, T. E. Smith, and G. Rein, "Review of emissions from smouldering peat fires and their contribution to regional haze episodes," *Int. J. Wildland Fire*, vol. 27, no. 5, pp. 293–312, 2018.

[75] C. E. Stockwell et al., "Field measurements of trace gases and aerosols emitted by peat fires in central Kalimantan, Indonesia, during the 2015 el niño," *Atmos. Chem. Phys.*, vol. 16, no. 18, pp. 11711–11732, 2016.

[76] A. Datta and R. Krishnamoorti, "Understanding the greenhouse gas impact of deforestation fires in Indonesia and Brazil in 2019 and 2020," *Frontiers Climate*, vol. 4, p. 5, Feb. 2022.

[77] C. Elvidge, M. Zhizhin, K. Baugh, F.-C. Hsu, and T. Ghosh, "Methods for global survey of natural gas flaring from Visible Infrared Imaging Radiometer Suite data," *Energies*, vol. 9, no. 1, p. 14, Dec. 2015.

[78] P. H. Freeborn, M. J. Wooster, D. P. Roy, and M. A. Cochrane, "Quantification of MODIS fire radiative power (FRP) measurement uncertainty for use in satellite-based active fire characterization and biomass burning estimation," *Geophys. Res. Lett.*, vol. 41, pp. 1988–1994, Mar. 2014.

[79] J. T. Morisette, L. Giglio, I. Csiszar, and C. O. Justice, "Validation of the MODIS active fire product over Southern Africa with ASTER data," *Int. J. Remote Sens.*, vol. 26, no. 19, pp. 4239–4264, Oct. 2005.

[80] C. F. Schueler, T. F. Lee, and S. D. Miller, "VIIRS constant spatial-resolution advantages," *Int. J. Remote Sens.*, vol. 34, no. 16, pp. 5761–5777, Aug. 2013, doi: 10.1080/01431161.2013.796102.

[81] T. Schwarting, J. Mcintire, H. Oudrari, and X. Xiong, "JPSS-1/NOAA-20 VIIRS day-night band prelaunch radiometric calibration and performance," *IEEE Trans. Geosci. Remote Sens.*, vol. 57, no. 10, pp. 7534–7546, Oct. 2019.

[82] S. Lee, W. Wang, and C. Cao, "JPSS-1 VIIRS DNB nonlinearity and its impact on SDR calibration," in *Proc. SPIE*, vol. 9607, 2015, pp. 343–354.

[83] W. Wang and C. Cao, "NOAA-20 VIIRS DNB aggregation mode change: Prelaunch efforts and on-orbit verification/validation results," *IEEE J. Sel. Topics Appl. Earth Observ. Remote Sens.*, vol. 12, no. 7, pp. 2015–2023, Jul. 2019.

[84] P. H. Laskowski, "The traditional and modern look at Tissot's indicatrix," *Amer. Cartographer*, vol. 16, no. 2, pp. 123–133, Jan. 1989.

[85] J. D. Foley, F. D. Van, A. Van Dam, S. K. Feiner, J. F. Hughes, and J. Hughes, *Computer Graphics: Principles and Practice*, vol. 12110. Reading, MA, USA: Addison-Wesley Professional, 1996.

[86] B. Braden, "The surveyor's area formula," *College Math. J.*, vol. 17, no. 4, pp. 326–337, 1986.

[87] M. J. Wooster, B. Zhukov, and D. Oertel, "Fire radiative energy for quantitative study of biomass burning: Derivation from the BIRD experimental satellite and comparison to MODIS fire products," *Remote Sens. Environ.*, vol. 86, no. 1, pp. 83–107, 2003.

[88] S. Lama et al., "Quantifying burning efficiency in megacities using the NO_2/CO ratio from the tropospheric monitoring instrument (TROPOMI)," *Atmos. Chem. Phys.*, vol. 20, no. 17, pp. 10295–10310, 2020.